9-24-2010

A Microwave Radiometer for Close Proximity Core Body Temperature Monitoring: Design, Development, and Experimentation

Quenton Bonds
University of South Florida

A Microwave Radiometer for Close Proximity Core Body Temperature Monitoring: Design, Development, and Experimentation

by

Quenton Bonds

A dissertation submitted in partial fulfillment
of the requirements for the degree of
Doctor of Philosophy
Department of Electrical Engineering
College of Engineering
University of South Florida

Major Professor: Thomas Weller, Ph.D.
Venkat Bhethanabotla, Ph.D.
Kenneth Buckle, Ph.D.
Andrew Hoff, Ph.D.
Ashanti Johnson, Ph.D.

Date of Approval:
September 24, 2010

Keywords: Non-Invasive Sensing, Near-Field Radiometry, Near-Field Antenna Design, Electromagnetic Propagation and Modeling of the Human Body, Radio Frequency Tissue Phantom Development

DEDICATION

To the young man or woman who is unaware of the unimaginable possibilities, and exciting opportunities that exist in the fields of science, technology, engineering and mathematics (STEM). To my former students of The Calhoun School and Project Success Alternative Learning Center in Lowndes County Alabama. To Telender Edwards, whose letter inspired me to push on when: 1) I was unmotivated; 2) I was extremely tired in the wee-hours of the morning but still had work to do; and 3) at times I would ask myself, 'Why am I doing this?', as I fought through the pain of the process, and my very purpose for pursuing the PhD was brought into question. To the youth of the slums, barrios and ghettos around the world, and last but not least, to the students of the Accelerated Destiny Technology Institute: this dissertation is dedicated to you!

ACKNOWLEDGEMENTS

I would like to first thank the many organizations and fellowship programs that supported me throughout this process such as the FEF and McKnight, the NSF sponsored Bridge to Doctorate Program (BD), IEEE, UNCF-SP, and especially the NASA sponsored Harriet Jenkins and GSRP programs. Thanks to my church family at Without Walls International Church and Trinity Life Center for always believing in me. Moreover, I offer special thanks to my advisor, Dr. Thomas Weller. In addition to the technical skills and knowledge you have imparted into me during my tenure at USF, I have also become a better leader and husband as a result of watching and weaning from you over the past six years. Thanks to Dr. John Gerig for his assistance on the project and design of the 2nd generation sensor. To all of my ENB 412 colleagues, thanks for keeping things interesting. To Bernard Batson for making sure I was well taken care of, many years after my matriculation through the BD program. To my family, and mother especially, Ms. Debra Bonds, thank you for expecting nothing less than greatness out of me. To my mentor, Dr. Eric Maxwell whose wisdom, guidance and spiritual insight have been essential to my successes in the PhD program. To Anthony Spitalieri, and Brian Norris, thanks for making me realize that *I am* a world changer. And last but not least to my beautiful wife, how do I articulate how much of a help you've been during these final and most critical months of this dissertation process? The meals were phenomenal, your wisdom priceless, and your love indescribable. I love you Terinee Jade Bonds!

TABLE OF CONTENTS

LIST OF TABLES

LIST OF FIGURES

ABSTRACT

Presented is a radiometric sensor and associated electromagnetic propagation models, developed to facilitate non-invasive core body temperature extraction. The system has been designed as a close-proximity sensor to detect thermal emissions radiated from deep-seated tissue 1 cm – 3 cm inside the human body. The sensor is intended for close proximity health monitoring applications, with potential implications for deployment into the improved astronaut liquid cooling garment (LCG).

The sensor is developed for high accuracy and resolution. Therefore, certain design issues that distort the close proximity measurement have been identified and resolved. An integrated cavity-backed slot antenna (CBSA) is designed to account for antenna performance degradation, which occurs in the near field of the human body. A mathematical Non-Contact Model (NCM) is subsequently used to correlate the observed brightness temperature to the subsurface temperature, while accounting for artifacts induced by the sensor's remote positioning from the specimen. In addition a tissue propagation model (TPM) is derived to model incoherent propagation of thermal emissions through the human body, and accounts for dielectric mismatch and losses throughout the intervening tissue layers.

The measurement test bed is comprised of layered phantoms configured to mimic the electromagnetic characteristics of a human stomach volume; hence defines the human core model (HCM). A drop in core body temperature is simulated via the HCM, as the

sensor monitors the brightness temperature at an offset distance of approximately 7 mm. The data is processes through the NCM and TPM; yielding percent error values $\leq$ 3%.

This study demonstrates that radiometric sensors are indeed capable of subsurface tissue monitoring from the near field of the body. However, the following components are vital to achieving an accurate measurement, and are addressed in this work: 1) the antenna must be designed for optimum functionality in close proximity to biological media; 2) a multilayer phantom model is needed to accurately emulate the point of clinical diagnosis across the tissue depth; 3) certain parameters of the non-contact measurement must be known to a high degree of accuracy; and 4) a tissue propagation model is necessary to account for electromagnetic propagation effects through the stratified tissue.

CHAPTER 1

INTRODUCTION

Microwave radiometers have been used in a wide range of remote sensing applications such as astronomy, atmospheric science and geology; however in the past 35 years they have also been studied for use in the area of biomedical microwave sensing. Biomedical microwave sensing is the science of using Radio Frequency (RF) devices and instrumentation as a way of retrieving biological data from the human body. Microwave sensors can nondestructively measure and or quantify certain properties of objects in harsh or sensitive environments where direct contact to the object under investigation is unachievable [1]. One such environment is the human body, wherein the objects under investigation are internal tissue and organs. Advances in microwave radiometry have facilitated the use of RF technology in biomedical sensing applications by retrieving the electrical and thermal properties of human tissue and organs. As a result microwave radiometers have been used in cancer (brain, breast, thyroid, etc…) detection/treatment, hyperthermia, and biomedical imaging by means of microwave thermography [1] – [4].

As microwave radiometry becomes more prevalent in biomedical applications, this work explores the feasibility of a close proximity modality for non-invasive monitoring of human tissue. The aim of this work is research and development towards subsurface monitoring of absolute tissue temperatures from the near field of the human body. In an effort to diagnose core body temperature, we are particularly interested in

noninvasively measuring the thermal emissions radiated from blood-fatty tissue through layers of skin and muscle. RF tissue phantoms are implemented as the measurement test-bed to simulate the human body in normal and adverse conditions. The sensor is intended to be deployed inside the uniforms of servicemen or as a hand held device for non-contact monitoring of temperature differentials inside the human body. Therefore the radiometer and measurement test bed were configured to replicate a health sensor positioned a short distances (10 mm – 50 mm) from the body.

The goal is to identify, analyze, and mitigate the problems associated with close proximity, non-invasive health monitoring using radiometric sensors. Previous studies have shown that developing an application specific (human monitoring) sensor and anenna design are essential to achieving such goals in the on-body approach [5] – [7]. Based on our preliminary works, we have discovered that modeling of the propagation effects in the tissue and antenna-body near field is also vital, especially for the non-contact measurement. Therefore the antenna, measurement test bed, and associated propagation models developed for this work are the main contributions of this study.

1.1 Motivation

The current sensor is intended for integration into the astronaut Liquid Cooling Garment (LCG) to non-invasively monitor astronaut core temperature in the improved lunar extravehicular activity (EVA) suit. Transition from extreme environments during lunar missions could lead to large differences in skin surface temperature and core body temperature (Figure 1). To achieve thermal stabilization heat is discarded from the liquid cooling system through a network of tubes. Physiological studies have proven that skin

surface temperature alone does not provide an accurate estimate of core body temperature even with correction [8]. Therefore the inlet temperature of the EVA suit does not alone provide sufficient diagnostic data. As a result, sensors that measure the skin surface temperature and or inlet suit temperature such as thermistors, infrared-IR thermometers, or thermocouples, should be supplemented with additional measurement modalities which are capable of subsurface data extraction.

Microwave radiometry serves as a feasible solution since radiometric sensors detect electromagnetic radiation naturally emitted across the depth of the tissue/material under investigation (T/MUI) in the form of brightness temperature. By means of microwave thermography, the detected brightness temperature is used to generate thermal gradients of TUI. Hence, our prime focus is to noninvasively monitor human core temperature and variations thereof by analyzing the brightness temperature data extracted from the measurement. The current sensor is designed to operate within the L frequency band of 1 GHz – 2 GHz, a spectrum which permits sufficient detection of emissions from deep within the body. The theoretical detection depth is up to 30 mm, enabling thermographic measurements through layers of skin fat and muscle tissue [1]; as a result the extraction of core body temperature is possible with proper positioning. The long-term goal for this work is to expand the utility of the system to a network of radiometric sensors positioned throughout the uniform of astronauts or servicemen at clinical diagnostic points (i.e. wrist-pulse, chest-heart beat, and core-body temperature) for retrieving various physiological data from the body.

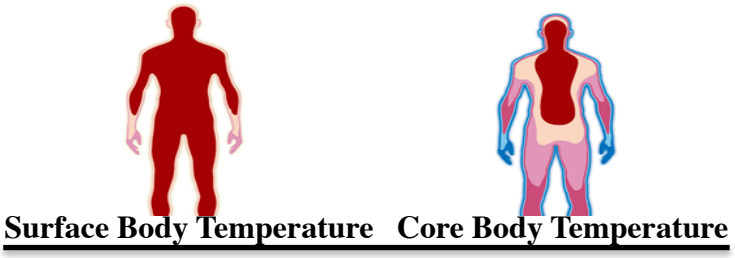

Figure 1. Surface body temperature (left) versus core temperature (right).

1.2 Contributions to the Practice

This study is expected to be the trailblazer for future works in area of close-proximity biomedical sensing and health monitoring using microwave radiometers. Subsequent contributions to the advancement of the practice have been made in the areas of antenna – sensor design for biomedical applications, RF tissue phantom development, electromagnetic propagation effects in the near field of the body and electromagnetic propagation throughout stratified tissue.

Close-proximity tracking of tissue temperature is conceptually demonstrated in the preliminary study of a total power radiometer (TPR), which is the 1st generation design. This initial study demonstrates the sensor design considerations from a biomedical sensing perspective. In particular, the effects of calibration, thermal stabilization, antenna – front end integration, and the design of the antenna itself, has a substantial effect on the accuracy of the measurement. These design considerations are employed in the development of the 2nd generation sensor, which incorporates various design enhancements that improve the performance of the sensor.

Measurement and testing is performed on RF tissue phantoms which have been designed to mimic the electrical properties of human skin, muscle, and blood-fatty tissue in the L frequency band. A notable contribution in this area is the development of a solid

skin-muscle phantom in composite form. Layered configurations of these phantoms are used to develop the human core model (HCM), which is believed to be the first phantom model configured to mimic a three dimensional volume of an abdominal cavity.

Some of the most significant contributions of this work are in the areas of antennas and propagation, as the antenna design has been deemed "critical" to the radiometric measurement. For this reason, we have identified the antenna requirements for biomedical radiometric sensing applications. We have also demonstrated certain near field propagation effects which distort the performance of the antenna at short distances from the body. An analysis of these near-field effects is used to design a cavity backed slot antenna (CBSA), with characteristics that circumvent these phenomena, enabling optimal sensor performance in the presence of human tissue. The CBSA has also been designed to meet the necessary requirements for microwave biomedical sensing.

In the context of electromagnetic propagation, there are certain artifacts that obstruct the close proximity measurement that cannot be accounted for in the antenna design. These artifacts are identified and a mathematical formulation in the form of a non-contact propagation model is derived to compensate for them. A sensitivity analysis is performed to determine the non-contact parameters to which the measurement is most sensitive.

A tissue propagation model (TPM) is developed to emulate the electromagnetic propagation effects, taking into account losses and dielectric mismatch as thermal emissions propagate through the body. The TPM presented and applied to the human core model (HCM), a physical representation of a conical stomach volume of skin, muscle, and blood-fatty tissue. The brightness temperature measurements for the HCM,

extracted by the radiometer, are correlated to the TPM. This provides an expression for the emitted temperature at the skin surface as a function of the emissions from the intervening layers. Ultimately, the core temperature can be resolved by solving for the muscle temperature in the TPM – radiometer expression, by applying heat transfer theory to the thermal profile of the tissue.

1.3 Organization of the Dissertation

This dissertation is organized into six chapters. Chapter 2 presents an overview of microwave radiometry theory, a review radiometric sensors design for biomedical applications, and justification for the close-proximity.

Chapter 3 presents a preliminary investigation of the 1st generation TPR to establish a benchmark measurement for comparison purposes throughout the remainder of the work. In this chapter, various tissue phantoms have been identified and characterized for testing purposes. An analysis of the antenna performance characteristics in the antenna-body near field is used to identify occurrences which impede the measurement. As a result, certain design methods have been implemented to compensate for these near-field effects. Ultimately, proof of concept is established in this chapter through successful tracking of a blood-fatty tissue phantom within the dynamic range of human body temperatures.

Chapter 4 presents the 2nd generation design, which incorporates enhancements to the sensor, antenna, and measurement test bed. Enhancements to the sensor include continuous calibration and miniaturization for improved performance. The antenna, a cavity backed slot antenna, is designed to preserve functionality in the presence of human

tissue. The measurement test bed is enhanced to a multilayer human core model (HCM) which mimics the electrical properties of an abdominal cavity across the depth of the tissue. The experimental setup is also presented in this chapter.

Chapter 5 presents the derivation of the non-contact model (NCM) which accounts for obstructive artifacts which further impede the close proximity measurement. A considerable improvement in accuracy is achieved after the experimental data from Chapter 4 is processed through the NCM. Thereafter, a sensitivity analysis is performed on the NCM parameters to identify the parameters the measurement is most sensitive to.

The tissue propagation model (TPM) is presented in Chapter 6 which models radiative transfer through the human body, accounting for losses in the tissue as well as dielectric mismatch. The NCM data is processed through the TPM towards an absolute temperature measurement. Lastly, the conclusions are drawn in Chapter 7 along with a discussion of the major findings of this investigation.

CHAPTER 2

A REVIEW OF MICROWAVE RADIOMETRY

2.1 Theory

Microwave radiometry is a branch of microwave sensing which provides a passive sensing technique for detecting naturally emitted electromagnetic radiation. Microwave radiometers are highly sensitive wireless receivers which detect noise power radiated from objects in the form of brightness temperature. The power density (P) emitted by the object is proportional to its brightness (T_B) and physical temperatures (T_{phy}) as demonstrated in (1), where e is the emissivity of the object, k is Boltzmann's constant and B is the bandwidth of the power density.

$$\begin{aligned} P &= kT_{phy}B \\ T &= T_B \times e \\ e &= \frac{T_B}{T_{Phy}} \\ T_B &= \frac{P}{ekB} \end{aligned} \qquad (1)$$

The theory of microwave radiometry originated in the 1920's when a scientist by the name of Max Planck discovered that all matter emits natural electromagnetic energy in his proof of "Plancks Law". He also discovered that this emitted energy is proportional to the frequency and temperature of the matter under investigation (MUI).

Planck's Law (2) provides a relationship between emitted energy, frequency and temperature.

$$Bf_{Planck} = \frac{2hf^3}{c^2}\left(\frac{1}{e^{\frac{hf}{kT}} - 1}\right) \quad (2)$$

Rayleigh Jean's Law is typically used in radiometric sensing applications, since it is an approximation of Planck's law, simplified for microwave frequencies. This is mainly due to the fact that the microwave band encompasses a small segment of frequencies within the electromagnetic spectrum (0 Hz – 10^{25} Hz), ranging from ~300 KHz – 300 GHz. It is also important to note that Rayleigh Jean's Law is normalized to a particular temperature, usually 300 ºK (80 ºF) which is essentially ambient temperature and provides a linear relationship between brightness temperature and frequency. Rayleigh's expression is provided in (3). Figure 2 illustrates a comparison of Planck's curves and Rayleigh Jeans curves at normal body temperature.

$$Bf_{Rayleigh} = \frac{2f_2kT}{c^2} = \frac{2kT}{\lambda^2} \quad (3)$$

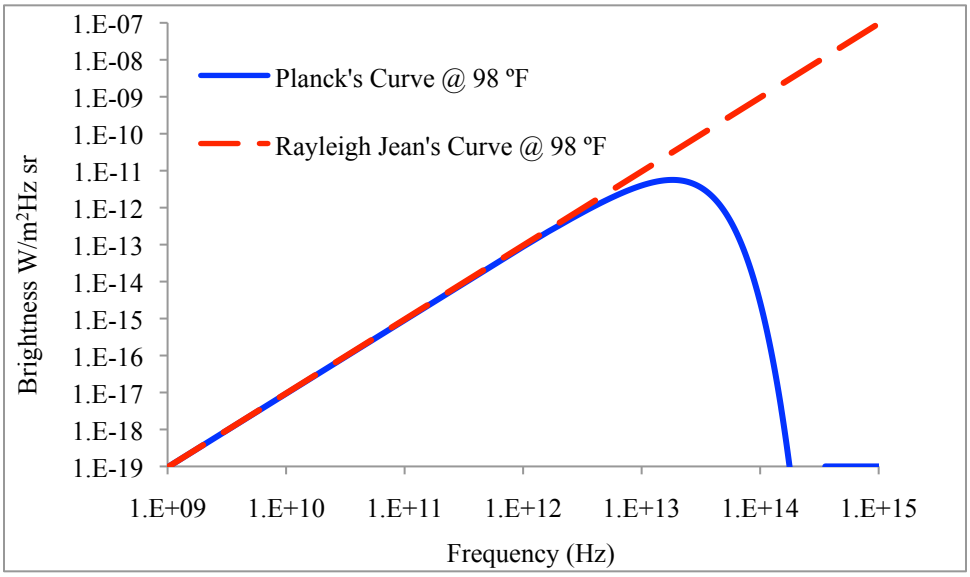

Figure 2. Comparison of Rayleigh Jean's law and Planck's law at normal body temperature 98 ºF.

2.2 Biomedical Radiometric Sensing

Microwave radiometers are likely to become common clinical instruments due to their vast range of applications such as oncology, surgery, gynecology, urology, mammography, just to name a few [1] – [7]. In particular, radiometers are used in microwave thermography as a means of generating thermal gradients of the MUI by quantifying the detected electromagnetic radiation which is in the form of emitted brightness temperature T_B.

The emitted brightness temperature is dependent the electrical properties of the object under investigation; i.e. permittivity, permeability, and conductivity. With respect to biomedical sensing the permittivity or dielectric constant is the most important [1]. Particularly the penetration depth is dependent on permittivity as a function of frequency. In general, materials with a lower permittivity allow deeper sensing depths. As described in [1] other useful relations can be made between water/oxygen content and permittivity;

such relations are the foundation for most microwave and radiometric sensors designed for biomedical sensing applications.

Permittivity is a measure of how much energy an object stores or dissipates amid an electric field. Permittivity is a complex number which varies with frequency; the real part denoting objects energy storage and the imaginary part representing the loss factor. In the presence of an electric field materials arrange their ions to receive energy from that field. The measure of how easily the electric field vectors permeate through the object for a given area is the permittivity which is determined by dividing the electric flux (D) by the strength of the electric field (E), and is measured in farads per meter (F/m), (4).

$$\varepsilon = \frac{D}{E} \tag{4}$$

The emissivity ***e*** is a constant which ranges from zero to unity, with unity being the emissivity of a perfect emitter implying that all of the power from the object is emitted. A perfect electric conductor (metal) has an emissivity of zero, implying that no power is emitted, but conducted through the material. Fresnel's equations demonstrate the relationship between emissivity and the electrical properties (permittivity) of human tissue (5) where Θ is the viewing angle of the sensor. This relation between power, emitted brightness temperature, and permittivity is expresses in, (1), (4) and (5). Similar relationships are used in analyzing biological data in biomedical microwave sensing [7].

$$e = 1 - \left| \frac{\varepsilon \cos(\Theta) - \sqrt{\varepsilon - \sin^2(\Theta)}}{\varepsilon \cos(\Theta) - \sqrt{\varepsilon - \sin^2(\Theta)}} \right|^2 \tag{5}$$

2.3 Contact Radiometry

A review of a few of the most significant contributions to on-body radiometric sensors is presented in this section. These radiometers demonstrate successes in the areas of blood glucose monitoring, cancer detection, and neurology. Considering that the majority of the research in biomedical radiometric sensing has been done in the area of breast cancer detection, the RTM-01-RES was selected for this review, since it is among the most extensively studied. Also presented is one of the most novel applications for the technology, a microwave radiometer designed for blood glucose monitoring. The objective of this study is to present previous successes in on-body radiometric sensing.

2.3.1 A Radiometric Sensor for Blood Glucose Monitoring

This study begins with one of the most interesting applications of biomedical radiometric sensing, blood glucose monitoring. In [7] Laura Ballew and researchers from the Baylor School of Medicine developed a microwave radiometer capable of tracking changes in blood glucose levels. Previous authors (E.C. Green [9]), have derived relations between blood glucose and permittivity. As stated in section 2.2 the brightness temperature is also related to permittivity. This work combines the relations between blood glucose, permittivity, and brightness temperature, and concludes that an increase in the radiometer brightness temperature is correlated to an increase in blood glucose levels.

2.3.1.1 Design and Specifications

Ballew's radiometer is a superheterodyne receiver with a Dicke calibration scheme. A rectangular waveguide was used as the antenna. The design frequency was

chosen to be within 4.5 – 6.5 GHz, yielding a penetration dept of 1 cm – 1.5 cm. This depth was chosen to facilitate the detection of blood flow in areas of low muscle content. The theoretical resolution of the radiometer is 0.2 °C (~0.36 °F) enabling the detection of subsurface temperatures with high accuracy. The device specifications were not measured, however the theoretical values are provided in Table 1.

Table 1. Theoretical design specification of Ballew's radiometer.

Parameter	Value
Frequency of Operation (GHz)	4.5 – 6.5
Pre-Detection Bandwidth (MHz)	600
Depth of detection of thermal abnormality (cm)	1 – 1.5
Temperature Resolution (°F)	0.065

2.3.1.2 Measurement and Results

The concept was demonstrated through the soda test, a standard experiment for blood glucose detection [9]. To implement the soda test, the wrist of the patient is firmly placed at the input of the radiometer. As the patient consumes a soda the brightness temperature of the radiometer is tracked up to one hour before and after consumption. The results of the soda test are shown in [7] which demonstrate an apparent increase in the brightness temperature over time. A similar plot is presented in Figure 3. These results imply that the radiometer was able to successfully track changes in blood glucose levels. However an absolute blood glucose measurement was not attempted. This research proved that radiometers can monitor variations in blood glucose; however more research should be conducted before characterizing microwave radiometers as clinical blood glucose sensors.

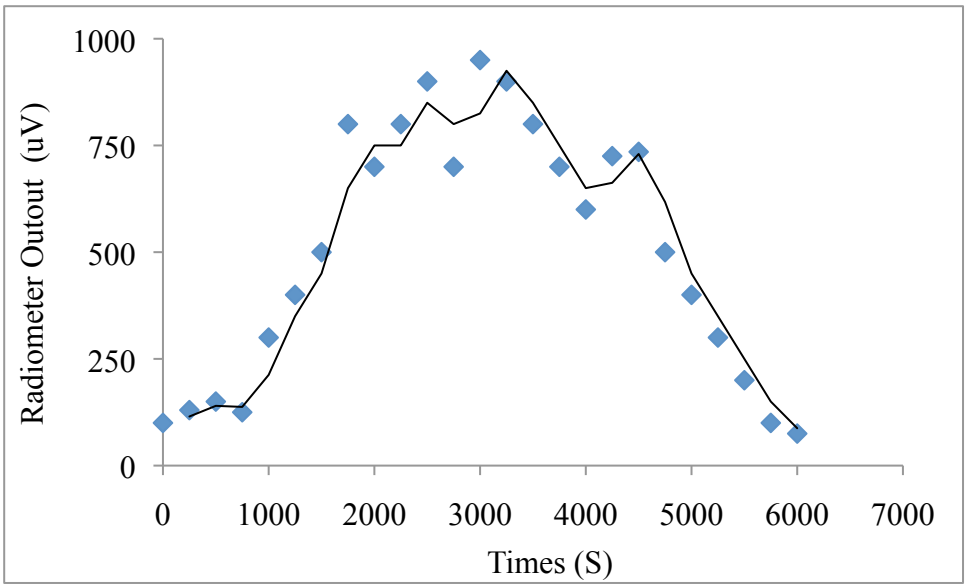

Figure 3. The radiometer output monitored as blood glucose level changes. The diagram was regenerated from [7].

2.3.2 RTM-01-RES

One of the most advanced radiometers developed for biomedical sensing applications is the RTM-01-RES, a computer based radiometer, capable of detecting abnormalities in human tissue and organs [5]. The RTM-01-RES was initially developed in 1996 by RES LTD, a company based in Moscow, Russia. Since its initial development, this radiometer has been engineered for a wide range of applications such as urology, gynecology, surgery, mammography, and IR thermography.

The RTM-01-RES has been most widely studied in the area of cancer detection, with most the work done in the area of breast cancer diagnosis. This is attributed to the fact that the RTM-01-RES can detect carcinoma in its pre-clinical stages. Palpation, mammography and ultrasonography are traditional clinical diagnostics used to diagnose anatomical disparities in the breast. However, research has proven that anatomical disparities in human tissue are preceded by physiological variations (temperature

differentials). In fact temperature changes may be caused by inflammation and increased cell metabolism, and are associated with degenerating tissue. The RTM-01-RES detects these psychological variations by generating temperature fields of internal tissue to detect malignant carcinoma at pre-clinical stages.

2.3.2.1 Design and Specifications

The RTM-01-RES is a Dicke radiometer with null balancing and a slipping circuit to reduce fluctuations caused by interactions between the biological object and the antenna. The frequency of operation is 1.15 – 3.8GHz. The device specifications for the RTM-01-RES are quite impressive (Table 2). The radiometer has a penetration depth from 3 cm – 7 cm depending on the dielectric properties of the tissue. The measurement range of internal tissue and organs ranges from 32 °C – 38 °C, which equates to 89.6 ºF – 100 ºF. The resolution of the radiometer is 0.2 °C (~0.36 °F) enabling the detection of temperature differentials with high accuracy.

Table 2. RTM-01-RES device specifications.

Parameter	Value
Frequency of Operation (GHz)	1 – 3.5
Pre-Detection Bandwidth (MHz)	100
Depth of detection of thermal abnormality (cm).	3 – 7
Temperature Resolution (°F)	0.36
Measurement Range (°F)	90 – 100

2.3.2.2 Measurement and Results

This section provides results from a RTM-01-RES diagnosis of breast cancer. The procedure is implemented with the patients lying on their backs with their hands behind their head, in order to normalize the positions of the measurement points of interest (flatten the breast). Ten evenly distributed diagnosis points on each breast are measured: the areola, centers of the quadrants, borders between the quadrants and auxiliary regions. The antenna is heated to the temperature of the subject for contact sensing, to bring the patients body temperature to a homogenous state. If the patient feels cold or uncomfortable the measurement could be distorted. The antenna is gently contacted on each of the points of interest for 20 s – 30 s on each breast. To maintain reliability, the points of interest are measured sequentially on the left then right breast. If the temperature differential between the investigation points of the left and right breast is more than ±0.8 ºF, there is a possibility of an error and the measurement procedure should be repeated. If such differentials are consistent, there is a high probability of abnormalities such as carcinoma in the breast, and or measurement area of interest.

The following diagnosis denotes a high risk of breast cancer:

1) *Increased thermal differentials between the corresponding of the left and right breast.*
2) *Increased thermal differentials between sites on the same breast.*
3) *Higher dispersion of the temperature differential between the left and right breast.*
4) *Differentials between the nipple sites of the breasts.*

5) High ductal (nipple) temperature in the damaged breast in comparison with average breast temperature, with respect to age.

Examples of internal temperature distributions for normal and cancerous breasts are shown in Figure 4. The right breast is diagnosed with ductal (nipple) cancer, and illustrates an elevated temperature in the ductal (middle) region of the breast.

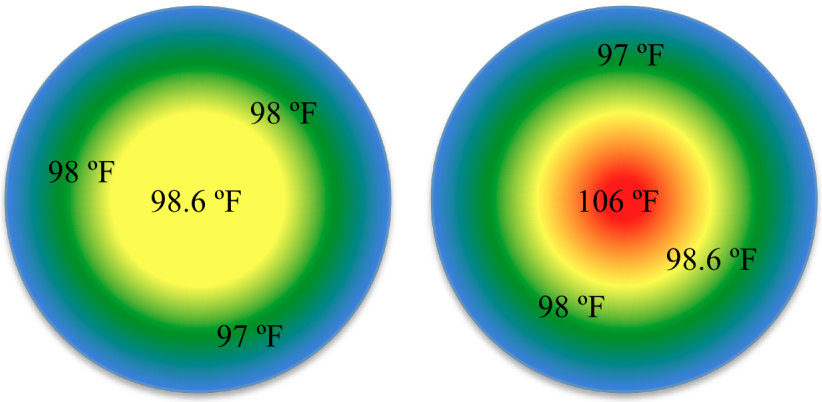

Figure 4. Thermal distribution of a healthy (left) and cancerous (right) breast. The diagram was regenerated from [5].

The RTM-01-RES also has implications in neurology, particularly in the treatment and monitoring of muscular disorders and the detection of spinal abnormalities. Figure 5 illustrates application of the RTM-01-RES in neurology by distinguishing spinal abnormalities. The red (dashed) line is a thermogram of a deforming spondileus of a 67 year old patient, which is compared with a thermogram of a healthy 21 year old patient with no abnormalities (blue).

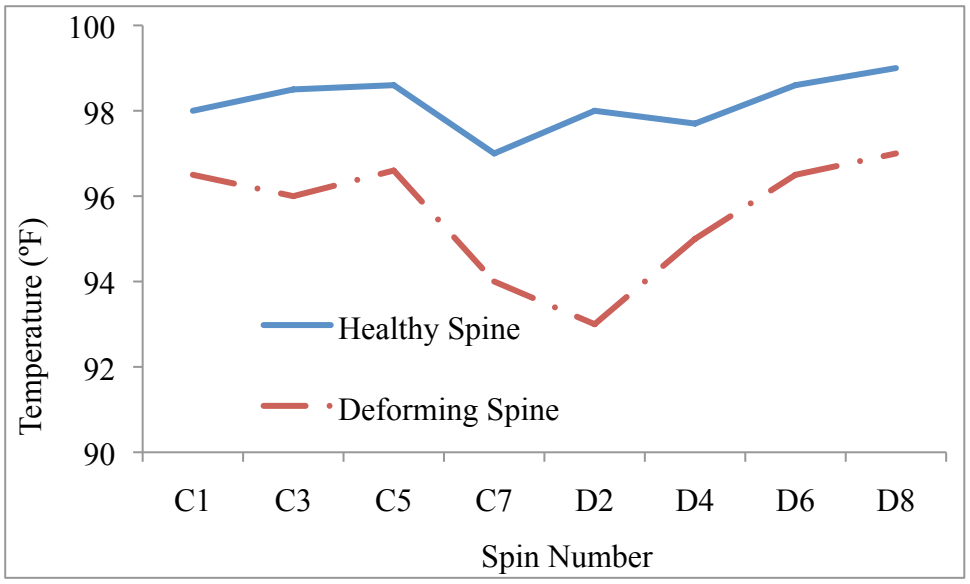

Figure 5. Thermogram of a deformed (red - dashed) and healthy spine (blue).

2.4 Limitations of the Contact Radiometry

Though on-body radiometric devices have been successful as biomedical sensors, there are some drawbacks that justify the need for a non-contact approach in certain applications. Recent studies (2006-present) have shown that there are several deployment issues specific to the on-body convention which may or may not be negligible depending on the application [10] – [12]. For instance, thermal conduction between the tissue and sensor can induce measurement uncertainties by distorting the temperature profile when the sensor is placed in direct contact with the body [5], [10], [12]. On-body sensors are also uncomfortable and may cause skin contusions under conditions of extended use.

Additionally, placing the antenna in direct contact with the tissue under investigation (TUI) creates near field diffusion wherein the detected fields are scattered throughout the TUI [10]. In the principle of core body temperature extraction, near field

diffusion limits the sensing depth which leads to detection of signals from areas closer to the tissue surface rather than the core. Though the area of maximum detected field strength is normal to the antenna with the *expected* Gaussian-shaped contour, thermal emissions from random areas within tissue induce measurement errors due to the degraded sensing depth. The recorded detection depths of actual on-body sensors are well below the theoretical limit, which could be partly due to the near field diffusion phenomenon [11]. The diffusion phenomena may be tolerable in cancer detection and or imaging applications where the brightness temperature of the specimen (i.e. cancer, brain activity, glucose variations) is distinguishable, being that its dielectric properties create stronger emissions than the surrounding tissue [4]. Though diffusion limits the detection depth, emissions from the specimen are 25%-35% stronger than the surrounding tissue and therefore detectable closer to the surface. However, in core body temperature extraction the dielectric properties of the tissue layers are relatively uniform across the lateral sensing profile. As a result the detected emissions are a function of the physical temperature of the specimen, which is at most 4% stronger than the surrounding tissue. Considering that healthy body temperature is approximately 98.6 ^{o}F with a dynamic range of ±4%, the human core emits weaker brightness temperatures that are difficult to detect due to the uniform dielectric profile of surrounding tissue. Therefore the degraded depth of detection induced by diffusion considerably impedes the ability to detect weaker subsurface temperature differentials emitted from the human core. Hence it can be argued that a non-contact approach is necessary to mitigate sensor placement issues, reduce measurement uncertainty, and enhance detection depth.

2.5 Non-Contact Radiometric Sensing

Recent successes in non-contact radiometry support the technological feasibility for true, non-invasive biomedical sensing [11] – [13]. As of late (2002-current), promising results have been achieved via remote (in this case, $d \leq 0.8$ m) monitoring of thermal and electrical conductivity variations of muscle and brain phantoms. In [12], a radiometric system is employed for intracranial imaging consisting of a directional antenna and/or array, and a large ellipsoidal cavity (1.5 m) for focusing microwave energy into the desired regions of the brain. A conformal antenna array and matching material between the antenna and specimen theoretically improves beam focusing to adequate detection depths for subsurface field imaging; the thickness of the matching material is crucial for optimal performance [12] – [13].

Of the current non-contacting modalities virtually none embody close proximity detection capabilities. The majority of the close proximity and near field measurement studies are in the preliminary stages, encompassing only simulation, theoretical, and conceptual demonstration. None of the previous studies have demonstrated an absolute subsurface temperature measurement at a range of a few centimeters from the TUI. The deficiency of a solid knowledge base within this area is essentially attributed to certain propagation challenges, which occur in the reactive antenna-body near field (Figure 6) such as electromagnetic (EM) field dispersion, antenna resonance shifts, bandwidth degradation, and impedance mismatch. Many authors have stated that these propagation challenges in the human body near field create daunting instabilities [11] – [14]. Others have identified these challenges as significant but very few solutions have been offered, other than to follow the on-body convention.

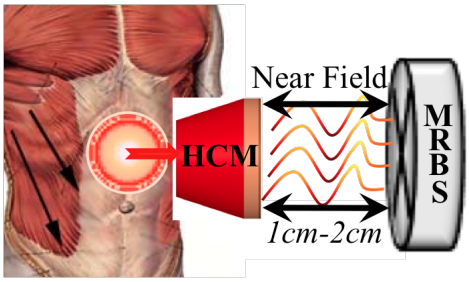

Figure 6. Radiometric sensor positioned in the near field of a human core model (HCM).

In [10] the near field dispersion phenomenon is explained and potential solutions are presented. The potential of close proximity brain imaging is investigated through simulation of electromagnetic field images across a cranium model. The latter demonstrates methodologies for maximizing resolution, detection depth, and sensitivity by means of application specific antenna design and proper antenna offset distance. Subsequent conceptual (simulation) studies imply that displacing the antenna precisely 10 mm – 20 mm from the specimen further improves the detection depth and pattern contour, beyond that of the matching layer approach mentioned in [13]. These simulations also demonstrate that precise offset minimizes near field diffusion. Though the results were promising, in-depth experimental studies are still necessary to characterize close-proximity radiometry as a viable biomedical sensing methodology.

CHAPTER 3

PRELIMINARY STUDY: THE 1ST GENERATION DESIGN

A conceptual demonstration of close proximity biomedical radiometry is demonstrated in this preliminary study of a total power microwave radiometer (TPR). The sensor is projected to be integrated into the uniforms of servicemen or as a hand-held device. Therefore, the radiometer and test bed are designed to replicate a health sensor positioned in close proximity (7 mm – 35 mm) to human tissue. The TPR was chosen for this initial study due to its relatively simple design which has been well studied in a broad range of non-invasive and or remote sensing applications; geo-science, remote monitoring of high temperature materials, and biomedical monitoring [15] – [18]. It is also the baseline design for more advanced radiometer architectures such as Dicke, Hach and noise injection [18]. This pool of prior knowledge reduces the number of unknowns when correlating the biomedical requirements of the close proximity approach to the sensor design parameters. In essence, some performance specifications can be estimated based on previous works. For instance, the TRR is designed for high resolution, with minimal components, which are desired characteristics for a stand alone or integrated health-monitoring device [17]. The drawbacks are sub-optimal accuracy and measurement uncertainty caused by gain drifts and instability in the low noise amplifiers [15]. Previous studies have proven that these phenomena can be mitigated through,

external calibration, device miniaturization and or thermal stabilization which will be implemented in Chapter 4.

One of the most significant contributions of this work is an analysis of the non-contacting nature of the sensor, which presents certain challenges that have been identified as substantial obstacles by previous authors (e.g. [16], [19]). Some of the most problematic design challenges are related to antenna performance degradation, as the antenna comes in close proximity to and or touches the body [19]. These phenomena are demonstrated by analyzing the performance characteristics of a printed dipole antenna in the near field of a blood-fatty tissue phantom. We propose various antenna design methodologies and near-field models to compensate for these effects. Until this work, very few solutions have been provided other than to follow the on-body convention, and none of the proposed non-contacting methodologies are feasible for a stand-alone device, capable of real time physiological monitoring.

Measurement and testing is performed on the test bed, which consists of a tissue phantom with the electrical properties (dielectric constant ε) similar to human tissue within the spectrum of 1 GHz – 2 GHz, which covers the frequency band of the TPR. In this initial study, we are particularly interested in noninvasively tracking temporal changes in a blood-fatty tissue phantom to demonstrate proof of concept. Tissue phantoms that mimic skin and muscle have also been identified to provide a more accurate model of the body. The applications of these phantoms models are limitless; biomedical telemetry devices, non-contact wireless sensors and wearable devices just to name a few. As the work progresses, layered configurations of these tissue phantoms will be configured to model the body's clinical diagnostic points, where the sensor is

expected to be positioned. These enhancements improve the accuracy of the test bed towards a clinical trial comparison. However the scope of this preliminary study is to first conceptually prove that biological data can be extracted from a simplified measurement test bed via close proximity total power radiometer measurements, identify the artifacts which obstruct the measurement, and provide solutions to mitigate these artifacts.

3.1 A TPR Designed for Biomedical Sensing Applications

The TPR design consists of an antenna, RF front end, down conversion stage, low frequency circuitry and a voltage detector for rectification. A block diagram of the TPR design is presented in Figure 7. The overall dimensions when placed inside of a metal enclosure for thermal stabilization are 50 cm x 9 cm x 4 cm. The sensor is essentially a high gain (~70dB) receiver that detects thermal emissions radiated from human tissue, which can be related to core temperature. The 1.4 GHz design frequency (f_c) enables an acceptable detection depth; up to 30 mm into muscle and blood, and 90 mm into fatty tissue [20]. The antenna is a printed dipole (PD) in a non-metal cavity designed at 1.4 GHz, with a 400 MHz bandwidth.

The next stage is the RF front end, a super-heterodyne receiver with the following components: multi-port RF switch, isolator, low noise amplifier, and band-pass filter. The switch connects to the antenna and two broadband (1 GHz – 18 GHz) reference temperature loads. Through calibration the reference loads are used to relate the signal at the radiometer input to an absolute temperature. A 50Ω termination submersed in cryogenics (liquid nitrogen) is used for the cold load (77 °K), while an attenuated diode

noise source is used for the hot load (~7618 ºK). The isolator attenuates unwanted noise emanating from the radiometer in the direction of the antenna, which may reflect off the specimen and or feed-back into the system input.

Next, the RF LNA is chosen to have a very low noise figure (NF < 0.6 dB), since the NF determines the input noise temperature of the first amplifier, which has a substantial effect on the overall noise temperature of the receiver (T'_{REC}) [18]. A noisy system can cause degradation in accuracy and precision since T'_{REC} is inversely proportional to the sensor resolution (ΔT). In particular T'_{REC} and ΔT are related by (6) where τ, β and T'_A are respectively, the sensor integration time, bandwidth, and noise temperature of the antenna. For this reason, a very low noise amplifier at the radiometer front end maximizes ΔT. High resolution sensors are vital for extracting subsurface tissue temperature, due to the fact that the dynamic sensing range could be as low as 10 ºF – 15 ºF. This range becomes even smaller, in the case of core body temperature extraction, as heat related disorders are diagnosed at ±5 ºF from homeostasis, 98.6 – 100 ºF. However, the primary function of the radio frequency (RF) low noise amplifier (LNA) is to aid in distinguishing the minimal detectable signal from the noise floor, by amplifying the emissions from the tissue under investigation (TUI). Since the human body temperatures are very close to that of ambient temperature, the RF LNA is chosen to have a high gain (30 dB) within the sensing band of interest (1.1 GHz – 1.6 GHz).

After amplification and filtering, a mixer with a 1.1 GHz local oscillator (LO) frequency performs double-sideband down-conversion to the intermediate frequency (IF). The low frequency circuitry consists of a low pass filter and two 21 dB gain IF LNAs, and is used to eliminate harmonics induced by down-conversion and amplify the input

signal to a suitable level for subsequent rectification. At this stage in the system the IF band is DC – 400 MHz. A DC block is added to protect the preamplifier from LO harmonics generated from down-converting. In the final stage, a Schotty diode is used for rectification of the IF band into a DC output voltage, proportional to the noise temperature at the radiometer input. The magnitude of the output voltage is then related to the intensity of the brightness temperature of the tissue under investigation (TUI), through calibration.

$$\Delta T = \frac{T'_A + T'_{REC}}{\sqrt{\beta\tau}} \qquad (6)$$

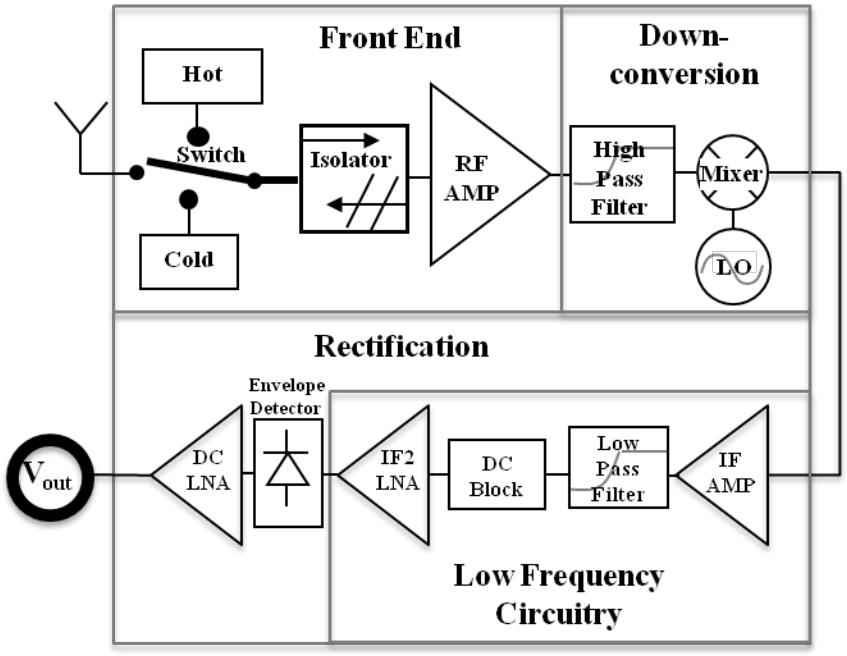

Figure 7. Block diagram of the TPR.

3.2 Calibration

The TPR employs an internal calibration methodology, wherein hot and cold references are measured to generate calibration curves. The calibration curves in Figure

8 were generated by two methodologies. It is important to note that the voltage offsets in the calibration curves in Figure 8, are likely due to positive amplification of the negatively polarized rectifier output. The first calibration methodology (CM1) makes use of a diode noise source for the hot load and a 50Ω load immersed in liquid nitrogen as the cold load. The reference noise temperature of the noise source and cold load are 1065 ºK and 77 ºK, respectively. A second calibration methodology (CM2) is implemented for comparison purposes, which uses a variable attenuator and a noise source, in which multiple calibration points are generated corresponding to temperatures ranging from 295 ºK – 7618 ºK. Theoretically if there are no gain variations in the system the calibration curves and equations for CM1 and CM2 should be identical. However, our results showed some variation in the slopes (system gain): 5.7 mv/K for CM1 and 4.9 mv/K for CM2. As a result gain variations are expected, which are likely due to suboptimal thermal stability of the front-end components. Since the total system gain is ~70dB, a small variation in gain could result in significant measurement uncertainties. Hence continuous calibration, and system stabilization are critical to achieving optimal accuracy and therefore will be included in 2nd generation sensor design.

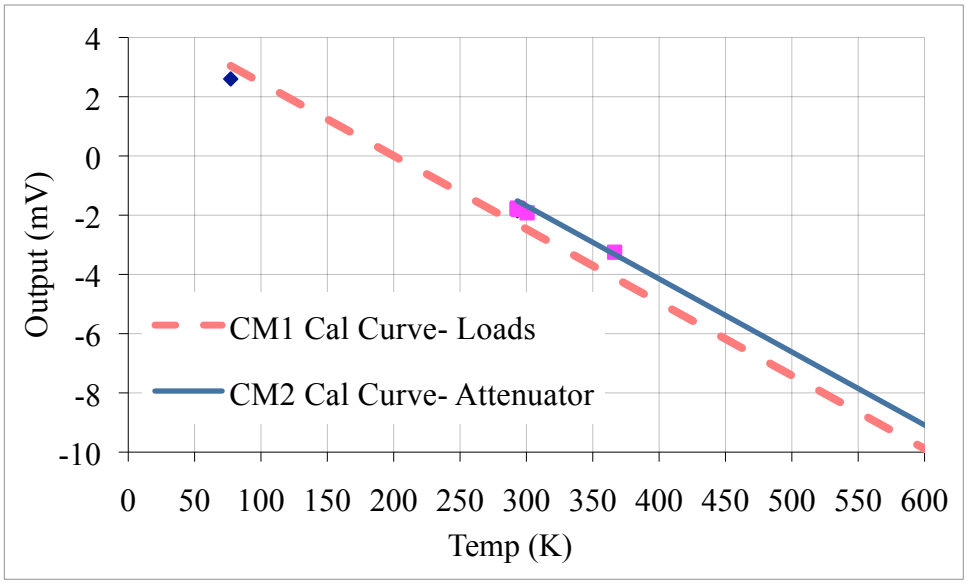

Figure 8. Calibration curves of the TPR.

3.3 Antenna Requirements for Biomedical Radiometric Sensing

Antennas designed for biomedical radiometric sensing are preferred to be high efficiency, directional radiators with broadband characteristics. A relatively compact directional radiator is preferred for targeted sensing of human tissue, organs, and or clinical diagnosis points (i.e. wrist-blood pressure, chest-heartbeat, core-body temperature). Though the size of the aperture is proportional to the directivity of the radiation pattern, it is inversely proportional to the frequency of operation which determines the sensing/detection depth. As a result there is a tradeoff between the antenna size, directivity, and sensing depth.

A broadband antenna enables maximum temperature resolution, which is critical in detecting subsurface emissions from internal tissue and organs. (1) defines the resolution and or minimum detectable signal of a radiometric receiver; where $T`_A$, $T`_{REC}$,

τ, and β are respectively the radiometric temperature detected by the antenna, system noise temperature, integration time, and bandwidth.

$$\Delta T = \frac{T'_A + T'_{REC}}{\sqrt{\tau\beta}} \qquad (7)$$

The sensor designer has very little control over $T`_A$. τ is the time needed for an accurate measurement of the TUI. Thus for the sensor to achieve high resolution, the antenna should be designed such that β is wideband at the sensor design frequency. The antenna should also exhibit a high efficiency which is critical in detecting low emissions from internal tissue. Any reduction in signal integrity caused by the antenna significantly degrades the accuracy of the sensor. Furthermore, an antenna with low efficiency heightens front end system loss by increasing $T`_{REC}$. T'_{REC} depends largely on the loss in the receiver front end and should be minimized to achieve maximum temperature resolution. Therefore a highly efficient antenna is preferred for optimal sensor resolution and accurate detection of weak emissions generated from human tissue.

3.4 The Printed Dipole Antenna (PD1)

A 1.4 GHz half wavelength printed dipole was selected for the TPR because it is a widely studied, compact, broadband aperture with a relatively simple design [21]. In our case a fairly compact, planar structure is preferred for ease of integration into uniforms or for deployment as a hand held device. An in-depth analysis of the 1st generation printed dipole antenna (PD1) is presented in this section. Figure 9 provides an illustration of PD1, which is designed using the Momentum full-wave electromagnetic simulator in Agilent's Advanced Design System (ADS). The front, side, and rear views of the

antenna are shown in Figure 10 and the dimensions provided in Table 3. The dipole arms are each λ/4 electrically, which is equivalent to a physical length of approximately 42 mm. The arms are fed by a λ/2 balun, which in theory balances the amplitude and phase of the current distribution between the dipole arms.

3.4.1 Characterization

The free space characterization in Figure 11 and Figure 12, shows that there is a very good agreement between the measured and simulated resonance, bandwidth (250 MHz), reflection coefficient (S11), and radiation pattern. As a result it can be inferred that the simulated and measured radiation characteristics (gain, directivity, and efficiency) are also comparable; these values are provided in Table 4.

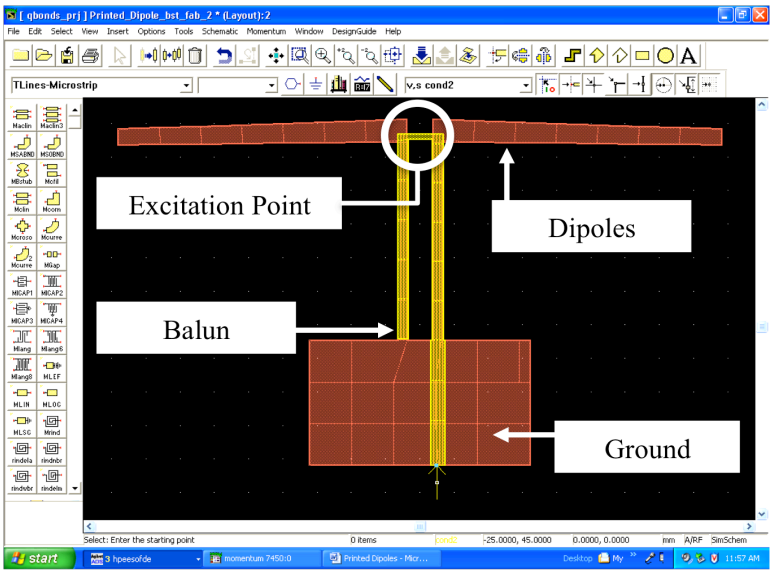

Figure 9. Momentum simulation of PD1.

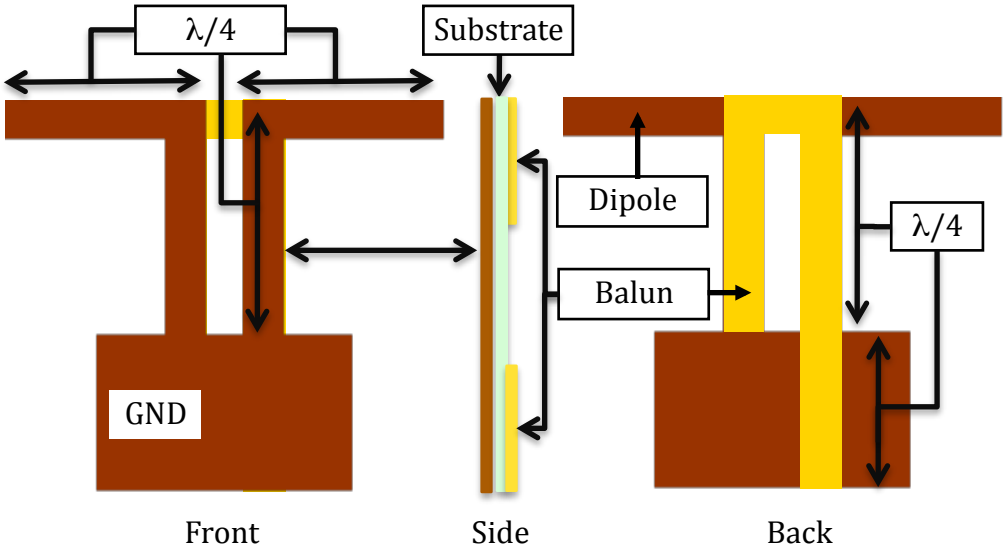

Figure 10. Front (left), side (middle), and back (right) views of PD1.

Table 3. Dimensions of PD1.

Parameter	Value
Overall Dimensions LxWxH (mm)	70x110x0.8
Height / Substrate Thickness (mil)	31
Length of λ/4 Dipoles (mm)	42x2
Length of Balun λ/4 Short and λ/4 Open (mm)	30.3x2
Ground LxW (mm)	32x19

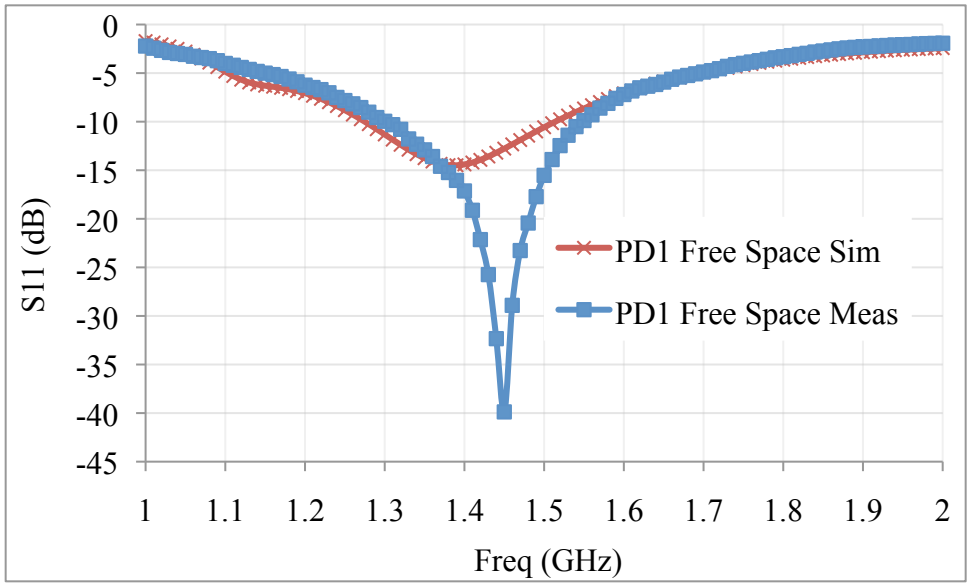

Figure 11. Measured versus simulated S11 of the printed dipole antenna in free space.

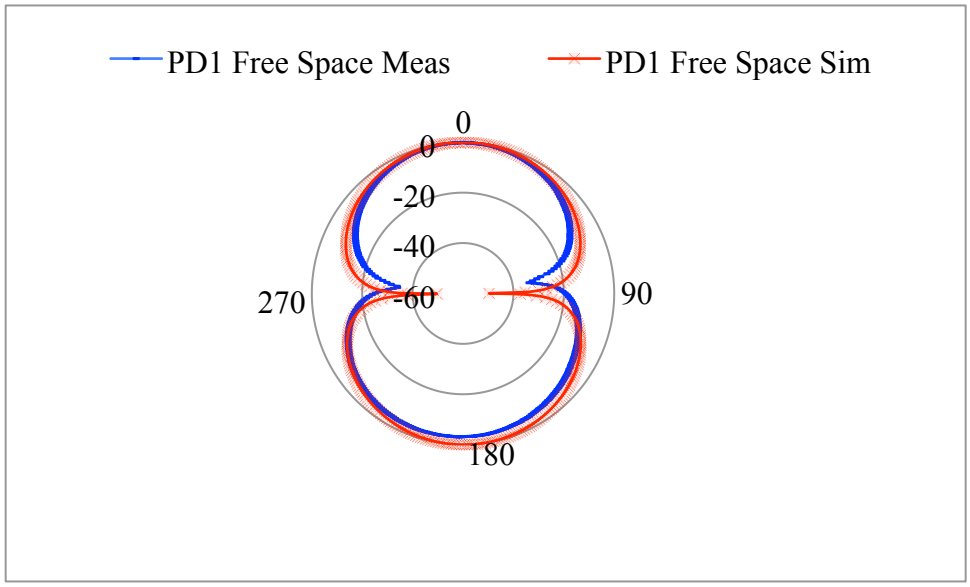

Figure 12. Measured versus simulated normalized radiation pattern of PD1 in dB scale.

Table 4. PD1 antenna characteristics.

Parameter	Value
Resonant Frequency (GHz)	1.45
Gain (dB)	1.56
Directivity (dB)	2.45
Efficiency (unit less)	0.85
Bandwidth (MHz)	250

3.4.2 Body Effects

As the antenna comes into the near field of the body, the antenna characteristics are distorted. Figure 13 demonstrates resonance shifts and antenna input match degradation, which arise from the antenna being at short distances (7 mm – 35 mm) from the TUI. More specifically, when the TUI – sensor offset is varied from 7 mm to 35 mm, the resonant frequency shifts from the 1.4 GHz design frequency to 1.5 GHz. Any divergence from f_c degrades the IF band input into the detector which subsequently reduces resolution, and in this case the depth of detection. In addition, the magnitude of the resonance is degraded by ~10 dB which would result in signal loss of at least 10% at the air – antenna interface. Most importantly, the bandwidth decreased from 250 MHz to 150 MHz when the antenna was brought within 7 mm of the TUI, which will degrade the sensor resolution, by a factor of at least 2. These characteristics will vary depending on the antenna, yet such losses considerably obstruct the accuracy of the sensor.

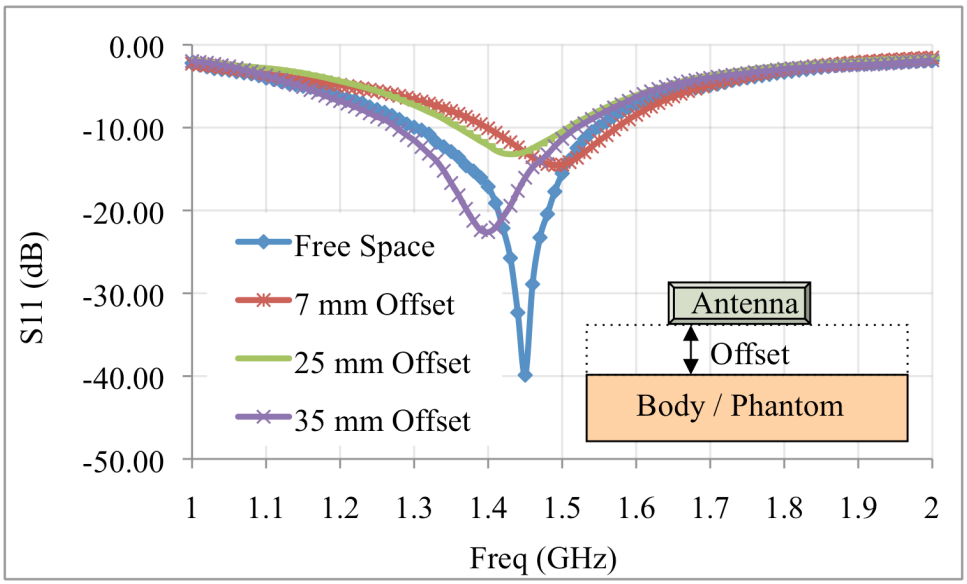

Figure 13. Antenna S11 degradation versus offset distance from the phantom.

3.4.3 Cavity Effects

The printed dipole generates an omni-directional radiation pattern (Figure 12), though a more directive pattern is desired in biomedical sensing applications [22]. A directional pattern could be achieved by adding a ground plane behind the dipole but the tradeoffs would be degraded bandwidth and increased aperture size, which are both undesirable characteristics for antennas deployed in biomedical applications [22]. For this reason a non-metal cavity was designed to isolate the antenna from background radiation (Figure 14). The cavity is comprised of Plexiglas, and lined with a near field absorbing material (supplied by ARC technologies[1]) designed to suppresses unwanted side and back lobe contributions by a factor of 20 dB. The cavity is adjustable such that tissue – sensor offset can be varied from 0 mm to 60 mm, enabling characterization of the sensor and antenna at distances representative of a health-monitoring device inside of an astronaut's uniform.

[1] ARC Technologies, 11 Chestnut Street, Amesbury MA 01913

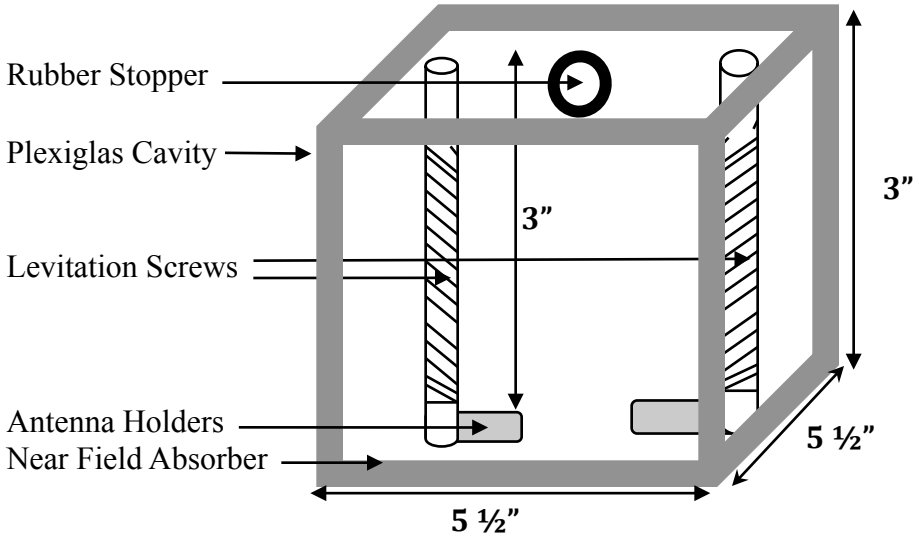

Figure 14. Non-metal cavity used for the printed dipole antenna.

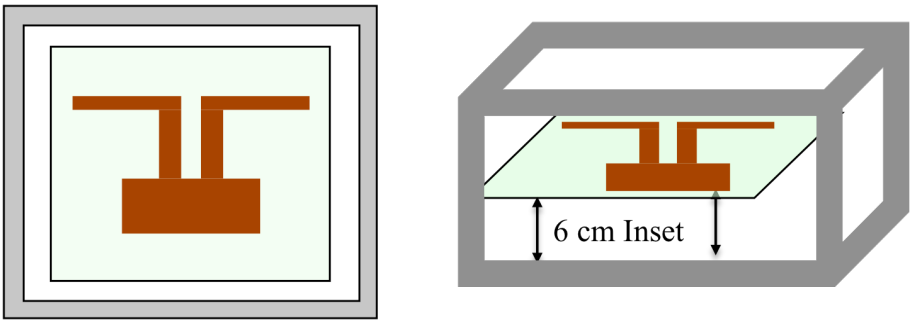

Figure 15. Bottom (left) and top (right) views of the PD1 inside the cavity.

Since the cavity itself induced changes in the antenna performance, the original printed dipole (PD) was redesigned (PD_{RE}) for optimal performance inside the cavity, by matching the impedance of the balun feed and tuning the dipole lengths for frequency selection. The orientation of the antenna inside the cavity is illustrated in Figure 15. The best performance was achieved with the antenna inset 6 cm inside cavity. Figure 16 shows the degraded S11 responses of PD1 in the cavity and the improved response of PD_{RE}. The dimensions of PD and PD_{RE} are described in Table 5.

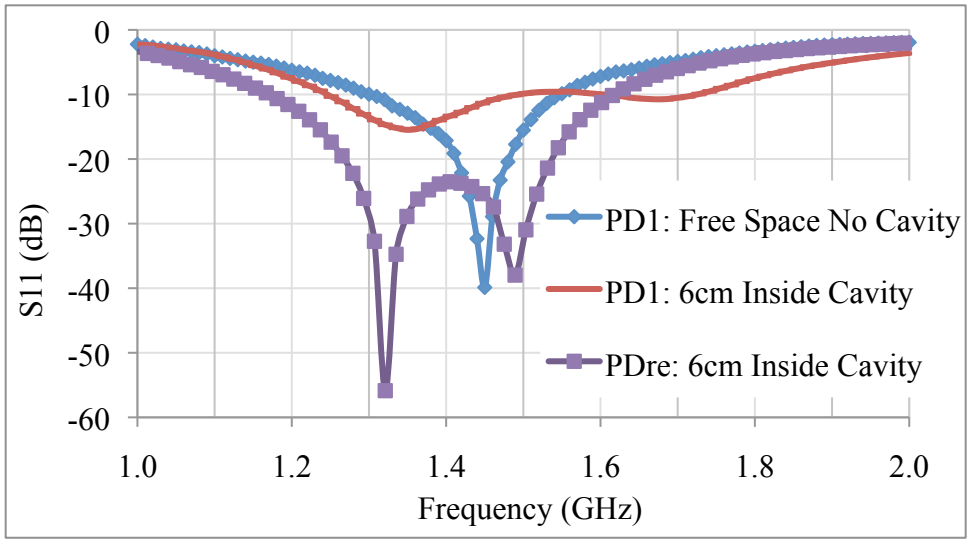

Figure 16. Cavity effects of PD1 versus PD_{RE}.

Table 5. Dimensions of PD and PD_{RE}.

Parameter	**PD**	**PD_{RE}**
Overall Dimensions LxW (mm)	70x110	70x110
Substrate Thickness (mil)	31	31
λ/4 Dipoles Length (mm)	42x2	47x2
Length of Balun λ/4 Short and λ/4 Open (mm)	30.3x2	30.3x2
Ground LxW (mm)	32x19	32x19

3.5 Measurement Test Bed

In order to benchmark the performance of non-invasive biomedical sensors, reconfigurable phantom models are needed which are capable of mimicking the physical and electrical properties of the tissue across the sensing depth. The body is a complex system, consisting of skin, muscle, blood and fatty tissue, with dissimilar electrical and physical properties. As a result, each tissue layer will affect the performance of the

sensor. Therefore, discrete phantoms, which model only one tissue layer at a time, do not provide the best replica of the body. To accurately depict the electrical profile of the TUI, layered phantom models must have a form factor similar to that of the tissue volume.

In this work various tissue phantoms have been developed and characterized which mimic the electrical properties of the intervening tissue layers of an abdominal cavity within the frequency band of 1 GHz – 2 GHz. However, only the blood phantom was used for simplification of the radiometric temperature measurement in this proof of concept demonstration.

The phantoms were characterized with respect to complex dielectric constant using the Agilent 85070E dielectric probe kit, and the results compared to the Gabriel model, which is used as the standard for human tissue characterization [23]. Since the tissue impedance is an important parameter for characterizing on-body sensors and near field antenna performance, the impedance of the phantoms were also calculated and presented in the analysis.

3.5.1 Blood-Fatty Tissue Phantom

Herein blood-fatty tissue was simulated using a mixture of hydroxethylcellulose (HEC), salt, sugar and water, the most prominent compounds in human blood as well as fatty (cellulose, salt, water) tissue (Table 6) [24]. To model blood and fatty tissue inside the stomach, a weighted average of the dielectric properties of the tissue is applied, assuming 12% body fat and 88% blood, which results in a dielectric constant of 53, and an impedance of 50Ω at f_c. Figure 17 outlines the development process, and the recipe is

provided in Table 8. As illustrated in Figure 18 and Figure 19, the blood phantom has a dielectric constant of 54 and impedance of 51Ω at f_c, which is equivalent to the findings of Gabriel and others in the literature.

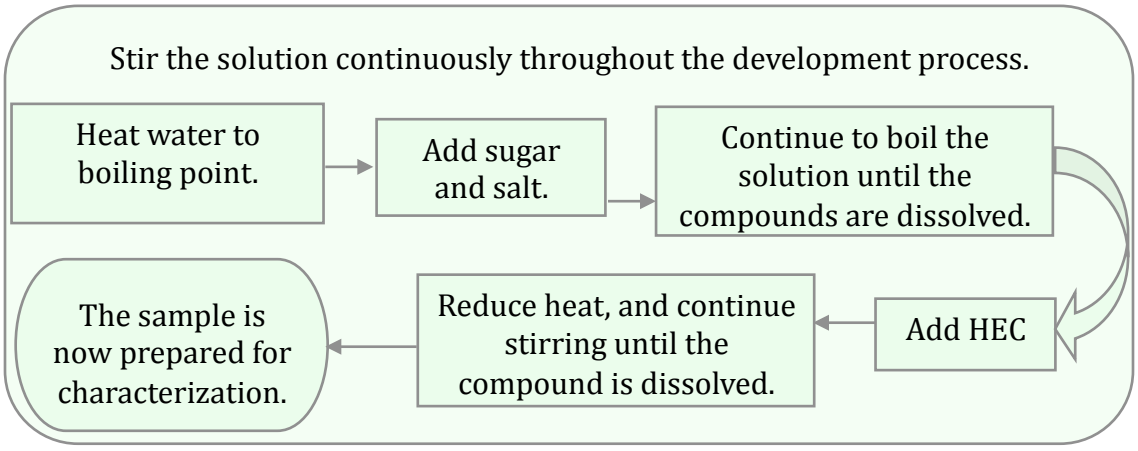

Figure 17. Development process for the blood-fatty tissue phantom.

Table 6. Recipe for blood-fatty tissue phantom [24].

Ingredients	**% By Weight**
Water	56
Sugar	0.76
Hydroxylethylcellulose (HEC)	41.76
Salt	1.21
Bactericide	0.27

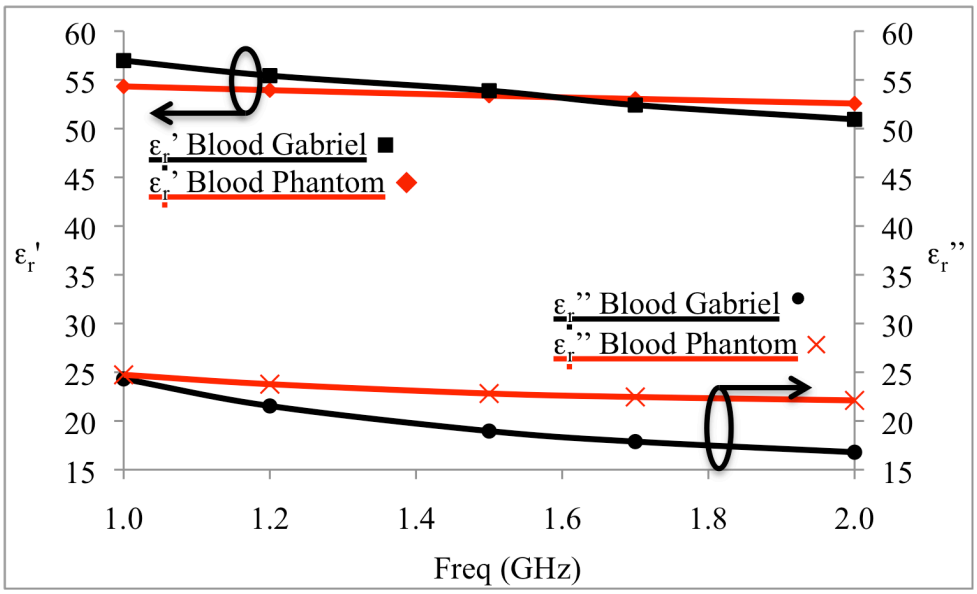

Figure 18. Comparison of the real (ε'_r) and imaginary (ε''_r) dielectric constant (ε_r) of the blood-fatty tissue phantom to the Gabriel model.

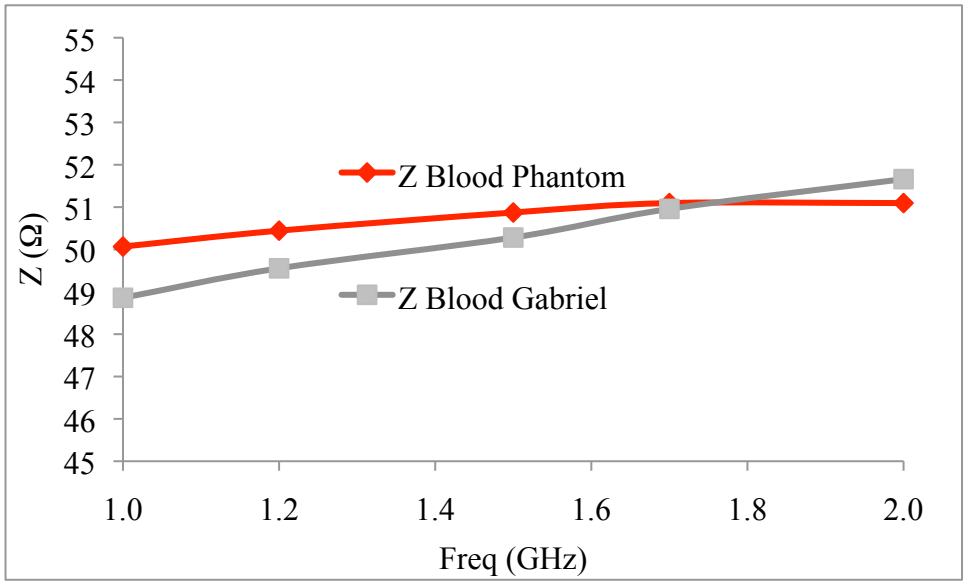

Figure 19. Comparison of the blood-fatty tissue phantom impedance (Z) to the Gabriel model.

3.5.2 Hybrid Skin-Muscle Phantom

Presented is the first hybrid skin–muscle phantom in a solidified composite form. As described in the introduction, the majority of the current tissue phantoms are discrete materials, usually liquids, whereas the human body is compromised of layered volumes of interconnected solids as well as liquids. Composite or hybrid phantoms provide a more accurate model of the body's clinical diagnostic points, which is important in improving the precision of the measurement test bed, as it is very difficult to model such a complex biological systems as the human body. Solid phantoms can be shaped into three dimensional volumes of human tissue without the support of casts or containers which may alter the relative dielectric, and or impedance profile of the phantom.

The skin-muscle phantom in Figure 20 is developed using a simple mixture of 44% water and 56% TX-151, provided by the Oil Center Research[2]. The process is presented in Figure 21, and the recipe in Table 7. The surface of the hybrid phantom mimics damp skin, to account for perspiration in conditions of extreme heat and or condensation deposits in cold environments. The skin layer has non-uniform thickness, ranging from 1 mm – 2 mm, which is comparable to the combined thickness of the dermis, epidermis, and hypodermis. The muscle layer is located immediately below the skin layer, and also has a non-uniform thickness of 7 mm to 8 mm. The electrical characteristics of the skin and muscle layers are presented below in Figure 22 – Figure 25. When preserved in an airtight enclosure, the electrical and physical characteristics of the phantom will remain relatively stable for at least 6 months.

[2] Oil Center Research, 616 W. Pont Des Mouton Road, Lafayette LA 70507

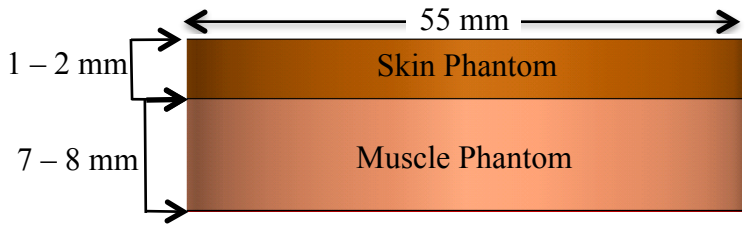

Figure 20. The hybrid skin-muscle phantom.

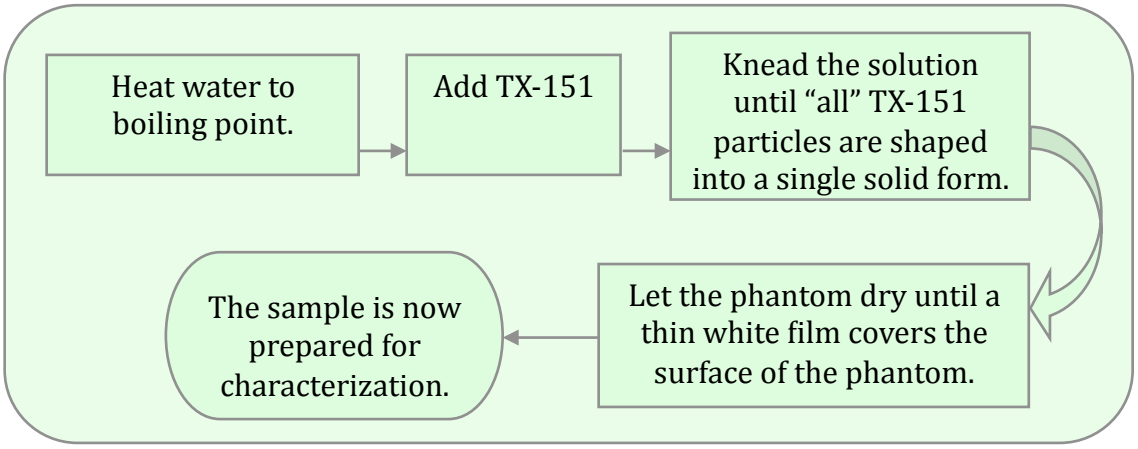

Figure 21. Development process for the hybrid skin-muscle phantom.

Table 7. Recipe for hybrid skin-muscle phantom.

Ingredients	% By Weight
Water	60
TX-151	40

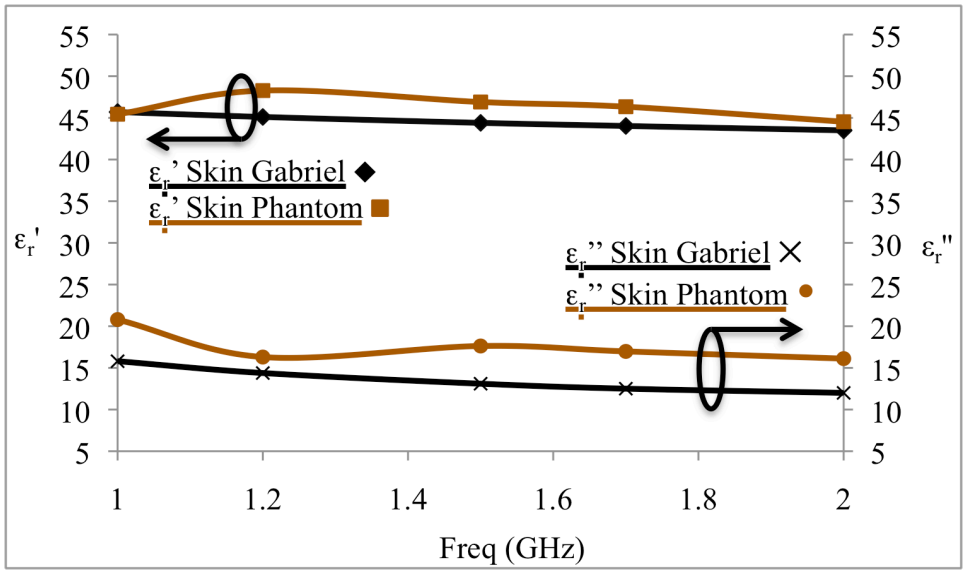

Figure 22. Comparison of the real (ε'_r) and imaginary (ε''_r) dielectric constant (ε_r) of the skin phantom to the Gabriel model.

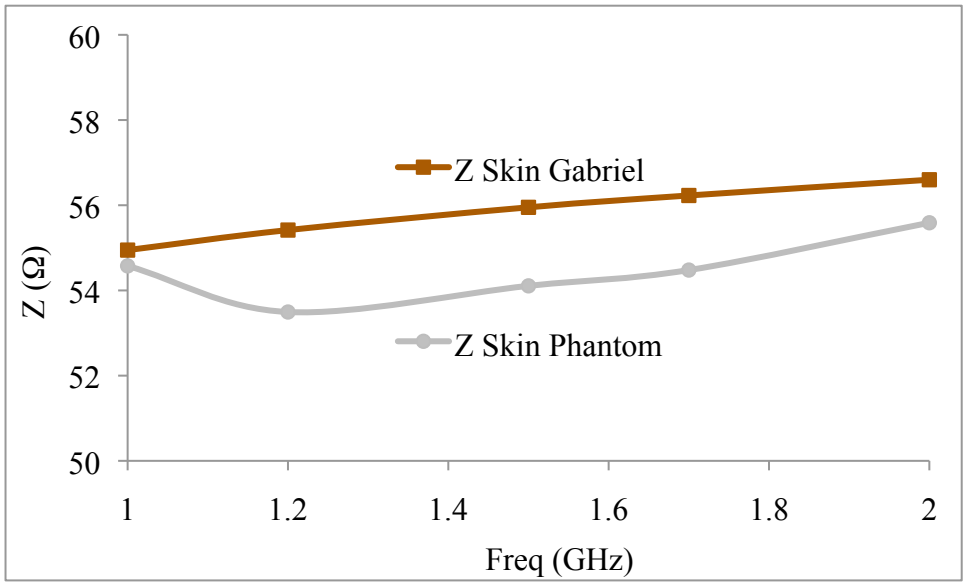

Figure 23. Comparison of the skin phantom impedance (Z) to the Gabriel model.

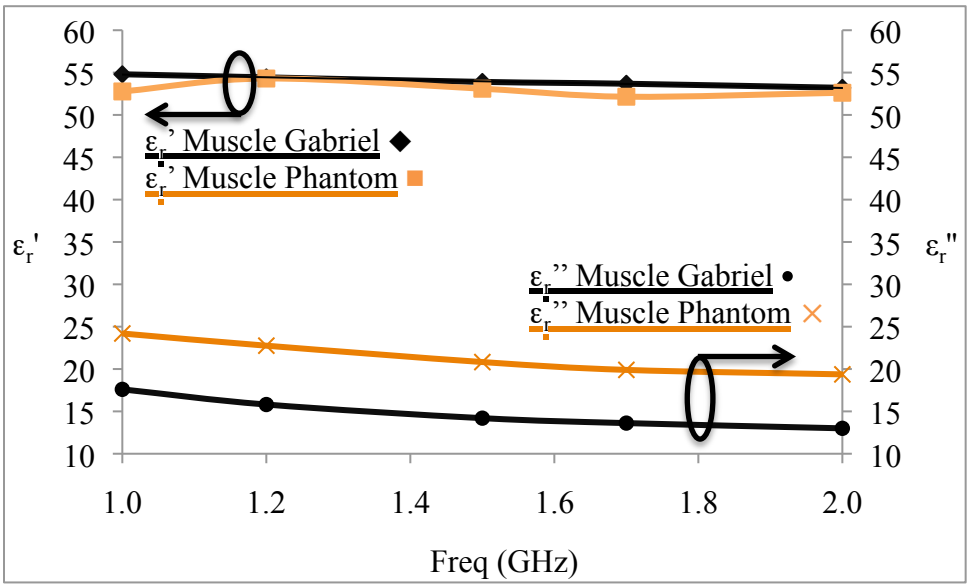

Figure 24. Comparison of the real (ε'_r) and imaginary (ε''_r) dielectric constant (ε_r) of the muscle phantom to the Gabriel model.

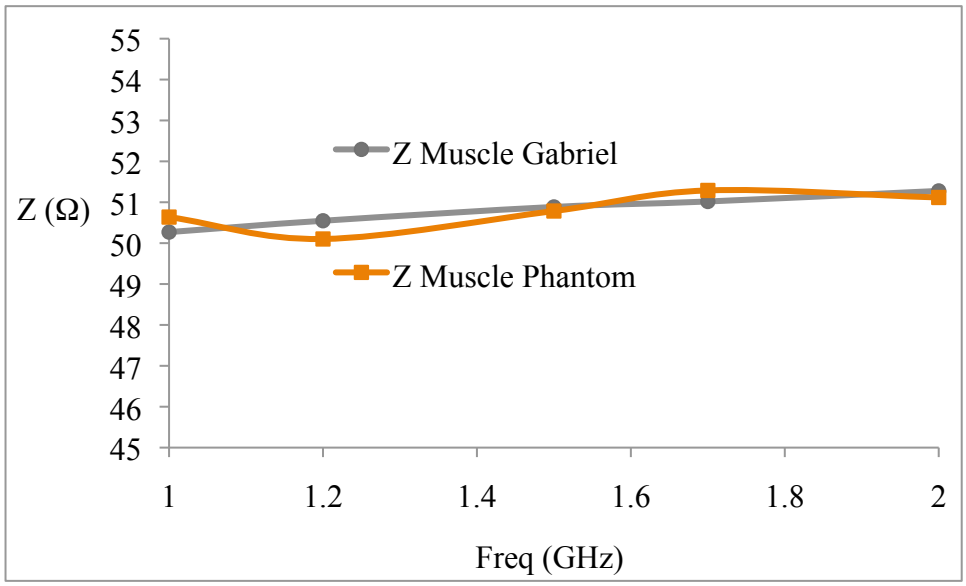

Figure 25. Comparison of the muscle phantom impedance (Z) to the Gabriel model.

3.6 Measurement Results

Referring to the measurement setup illustrated in Figure 26, the temperature of the blood phantom was varied as the radiometer monitored the brightness temperature with

the PD_{RE} positioned facedown inside the cavity, parallel to the TUI, offset ~25 mm from the phantom (Figure 15). The physical temperature is tracked using an infrared thermometer (IR) at the surface of the phantom and a digital thermometer (DT) located internally, at a depth of ~50 mm. In an effort to simulate a drop in core body temperature, the phantom temperature was varied from 111 °F to 65 °F, which is just outside the dynamic range of human body [25]. Human core temperatures (T_c) in the range of 93 °F < T_c < 101 °F are considered normal. Temperatures outside this range are considered adverse with T_c < 93 °F being Hypothermic, and $T_c \geq$ 102 °F considered exhaustion or heat stroke.

An analysis of the experimental data, showing the comparison of temporal variations between the TPR, the IR and the DT, is provided in Figure 27. The curves in this figure are normalized to the initial temperature reading of the TPR. The internal and surface temperatures of the phantom are virtually identical which implies that the phantom temperature is uniform throughout. The similarities in the curves prove that the TPR indeed demonstrates the general ability to track changes in tissue temperature from the near field of the TUI. However, there are some differences in the morphology of the TPR curve as compared to the IR and DT. In particular, the slope changes in the radiometric curve exhibited in time intervals 3 and 6 are likely due to spurious signals detected in the antenna back lobe. They could also be an effect of amplifier gain drifts, which were predicted from the results of the calibration analysis in section 3.2. In addition the radiometric measurement appears to be colder than the IR and DT which is likely due to factors relating to the non-contacting nature of the sensor, e.g., reflection loss at the antenna input, back/side lobe contributions, air-skin reflections, noise radiated

by the receiver, and the emissivity of the specimen. These artifacts contribute to the radiometric measurement and are heightened in close proximity sensing applications.

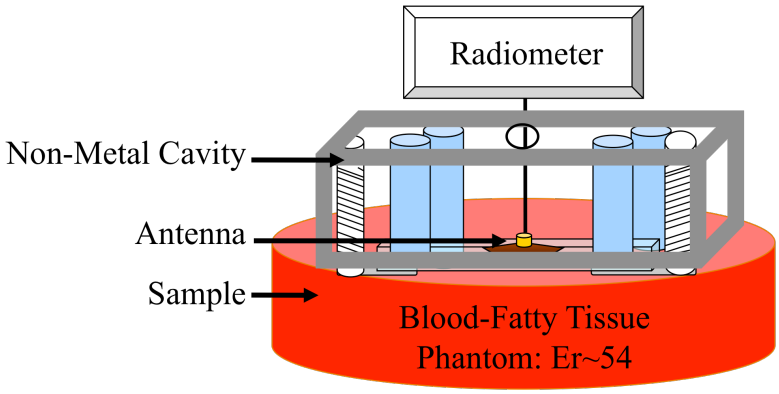

Figure 26. 1st generation measurement test bed.

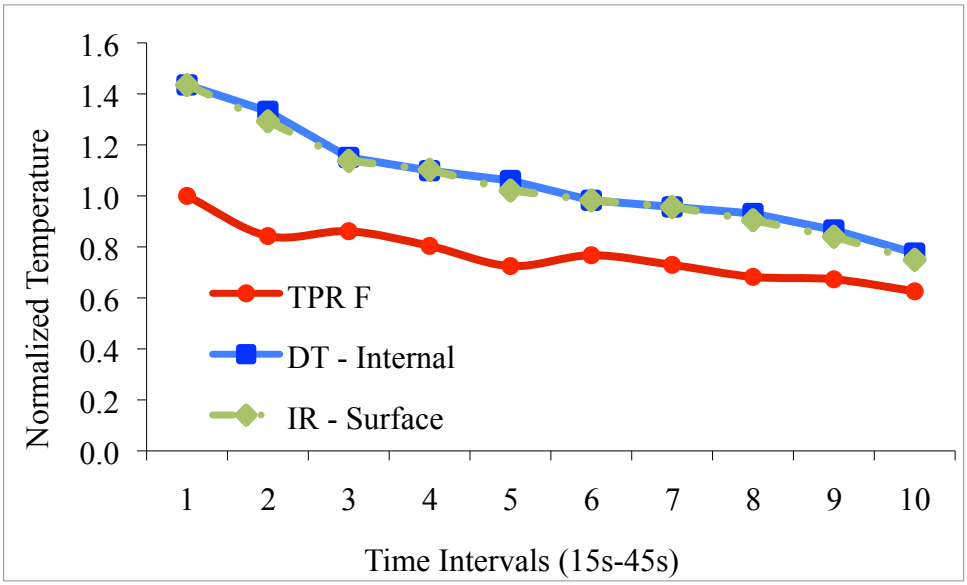

Figure 27. Results – normalized phantom measurements: TPR vs infrared thermometer (surface) and digital thermometer (internal).

3.7 Conclusion

Presented is the initial development of a radiometric sensor for noninvasive, close proximity biomedical monitoring. Although the ability to track temporal changes in the specimen temperature has been qualitatively demonstrated, certain phenomena have been identified which distort close proximity radiometric measurements. The measurement results imply that absolute specimen temperature extraction is plausible, however a mathematical model is necessary to account for certain artifacts which arise due to the non-contacting nature of the sensor. Solutions in the area of antenna design are provided, by implementing an absorbing cavity to suppress unwanted radiation opposite the TUI, and designing the antenna for optional functionality in close proximity to the body. We have also identified receiver instability characteristics which are represented by the variations in the slopes of the calibration curves and are likely due to thermal drifts in the RF components. The proposed solutions are a miniaturized design with an enhanced calibration scheme and thermal stabilization. Hence a 2nd generation design is presented in CHAPTER 4, which incorporates continuous calibration to mitigate receiver instabilities and an improved antenna design to compensate for the near field effects.

CHAPTER 4

2ND GENERATION DESIGN

This chapter presents various enhancements to the sensor and antenna design, to mitigate certain artifacts which obstruct the close proximity measurement. Experimentation and testing are performed on an enhanced measurement test bed, a multilayer phantom model which mimics a three dimensional volume of an abdominal cavity. The modifications to the 1st generation sensor facilitates improved accuracy and resolution by means of a miniaturized design which incorporates a continuous calibration scheme. The most noteworthy enhancement is the 2nd generation antenna, in which its novelty lies within the performance characteristics that aid in preserving the functionality of the sensor in the antenna-body near field.

4.1 Design of a Microwave Radiometer for Biomedical Sensing (MRBS)

The (MRBS) is a continuous calibrating TPR with direct conversion (D – C) in-phase (I) quadrature (Q) demodulation, I/Q. When compared to the superheterodyne based TPR, the advantages of the D – C I/Q architecture are reduced cost, power consumption, radio frequency components, and high linearity [26]. Most importantly, the architecture is well suited for miniaturization. These characteristics are ideal for the intended application, a stand alone health monitoring device, integratable into the uniforms of astronauts or servicemen for core body temperature monitoring.

The design consists of a cavity backed slot antenna (CBSA) [22], RF front end, and I/Q channels with an integrated rms detector. The block diagram is shown in Figure 28. Analogous to the TPR, the MBRS design frequency is 1.4 GHz which in theory, provides sensing depths up to 30 mm through skin, muscle, tissue [20], enabling the measurement of the blood temperature beneath the abdominal cavity. The antenna is a CBSA, designed for optimal functionality in close proximity to the body. The front end consists of a multi-port RF switch, isolator, low noise amplifier, and band-pass filter. The switch connects to the antenna and three reference temperature loads. A 50Ω termination at room temperature is used for the cold load (71 ºF), while an attenuated diode noise source is used for the hot load (235 ºF). The third standard is an open circuit, which is used to determine the noise temperature generated by the radiometer in the direction of the antenna (T_{REV}) and or reflected back into the system (T'_{REV}). An L-Band isolator is used to attenuate $T_{REV,}$ while in effect the noise temperature of T'_{REV} is equivalent to the physical temperature of the isolator. The final component in the RF front end is the band-pass filter, which has a center frequency of 1.4 GHz with a 100 MHz bandwidth. The band pass filter attenuates spurious signals outside of the sensing band of interest and passes the signal contributions emitted across the targeted detection depth.

After amplification and filtering the signal is equally divided into the I and Q channels for D – C demodulation ($LO = f_c$), and subsequent rms rectification to DC output voltages. The schematics of the I/Q channels are equivalent to the low frequency circuitry in the first generation design presented in section 3.1 In general, I/Q demodulation involves direct conversion D – C at the design frequency (f_c) via two

mixers with the local oscillator frequencies synchronized to f_c, and 90º out of phase, thus the term in-phase quadrature. As a result the image frequency is centered at 0 Hz and both positive sidebands are preserved in the I and Q channels, as the negative sidebands and respective harmonics are canceled and or filtered. In theory the I and Q outputs are combined to reconstruct the double-sideband signal, however only one channel is considered in this study for simplification.

Compared to the TPR architecture, the overall size reduction of the MRBS allows for enhanced stability, resolution, and accuracy. The dimensions of the MRBS are 22 cm x 6.3 cm x 4 cm which equates to a size reduction of about 50%, when compared to the 1st generation TPR (50 cm x 9 cm x 4cm) initially presented in section 3.1. Thermal stabilization is more efficient and easier to implement on smaller devices with fewer components, as a result the accuracy of the sensor is improved substantially. Thermal stability of the MRBS is achieved by a metal enclosure. The signal transmission path is also shortened, which reduces front end losses that contribute to the receiver noise temperature (T'_{REC}). The result is improved resolution, as T'_{REC} and ΔT are inversely proportional, (6).

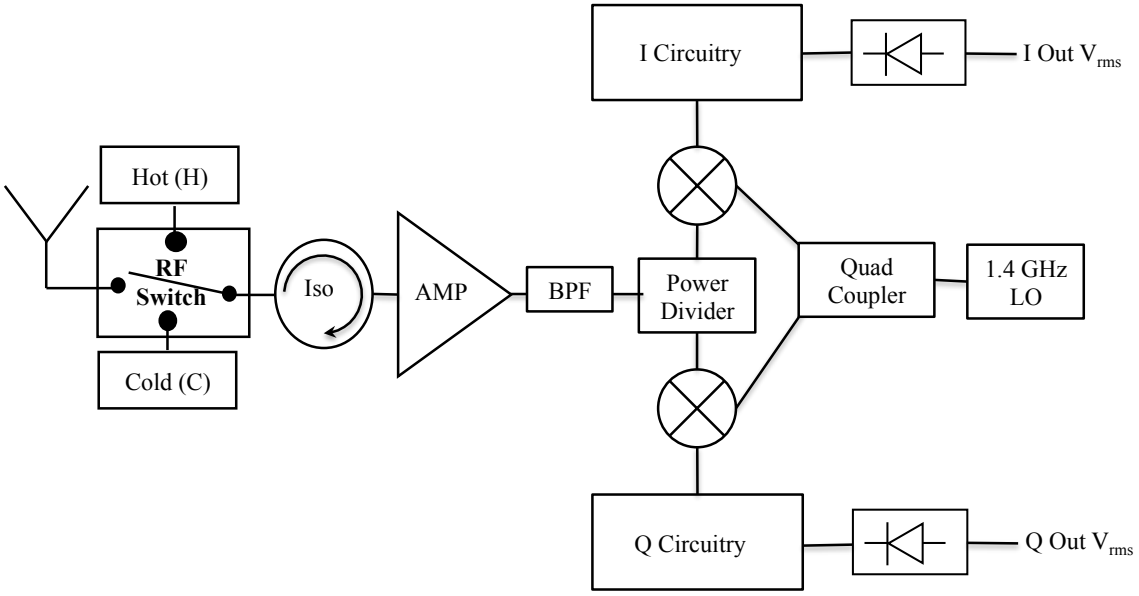

Figure 28. Block diagram of the MRBS.

4.2 Calibration

Continuous calibration is implemented in the MRBS design which minimizes measurement uncertainty and improves resolution. When compared to the TPR, in which only one calibration curve is generated per experiment, the MRBS generates a calibration curve for each T_B measurement. In effect, each data point is extracted with optimal precision, given that the noise temperature of the calibration standards are know to a high degree of accuracy. As described in the previous section, three standards are measured during each calibration cycle; hot T_H, cold T_C, and open T_O. The time interval for each cycle, including the specimen temperature T_{SC} (TUI) is approximately 1.3 s. The results is a substantial reduction in the allowable time window for gain drifts in the RF components, which in-turn minimizes measurement uncertainty. Continuous calibration also enables the detection of small temporal changes in the TUI, and therefore improves ΔT.

4.3 A Cavity Backed Slot Antenna (CBSA) for Near Field Biomedical Radiometry

The most noteworthy enhancement of the 2nd generation sensor is the antenna; a cavity backed slot antenna (CBSA), designed to satisfying the requirements for near field human body detection. By combining the advantages of annular slot and cavity backed antennas, the CBSA is designed to compensate for obstructive antenna-body effects, initially demonstrated in section 3.4.2 of the preliminary study. The antenna is a directional, broadband radiator, design at 1.4 GHz. It is also frequency tunable and or reconfigurable for implementation in other biomedical sensing applications.

Although spiral, patch, array, and other antennas commonly used in biomedical sensing applications were considered, the performance characteristics of cavity and annular antennas are best suited for the close proximity approach and provide better design flexibility. Multiple degrees of freedom in the antenna design are desired, mainly due to the varying performance characteristics in the near-field of the body. With respect to sensor performance, the main advantage of annular slot antennas over patch antennas is improved bandwidth. Conversely annular slot antennas generally radiate an omni-directional pattern due to the lack of a ground plane whereas a directive antenna with good efficiency is preferred in biomedical applications. A commonly used high efficiency directional antenna is a microstrip array but its large aperture size and narrow bandwidth at low GHz frequencies makes this antenna undesirable for the current application and design frequency. Therefore a probe fed cavity antenna is chosen for this study because it is a highly efficient, broadband, directional radiator which can be scaled in size by introducing a dielectric fill.

4.3.1 CBSA Design Concept

The CBSA consists of an annular slot antenna in contact with a cylindrical metal cavity [27]. The CBSA dimensions are given in Figure 29. The cavity is filled with a Teflon dielectric, and excited by an internal coaxial probe. The internal probe excites the inner patch of the annular slot aperture. Frequency tuning of the antenna is another important feature of the internal probe, enabling detection at multiple sensing depths. Tunable antennas are especially useful in the biomedical arena for detection of multiple clinical diagnostic points. Implementation of the cavity further improves antenna bandwidth, gain, directivity, and suppresses surfaces currents while forcing radiation in broadside direction towards the TUI. The dielectric fill allows for reduced aperture size, and lower frequency operation. An adjustable specimen holder is integrated on top of the cavity which regulates the distance between the phantom and antenna from 7 mm – 25 mm, the estimated distance between the body and projected health monitoring device.

Symbol	Dimension	Size (mm)	
W	Width of Slot	10	
ρi	Inner Conductor Radius	21	
ρo	Outer Conductor Radius	45	
L	Feed Length	48	
D	Cavity Depth	27	
D	Teflon Fill Depth	25	
W	Width of Slot	10	
	Crossed Slots LxW	24x2	20x2
	Short LxW	12.5 x 6	

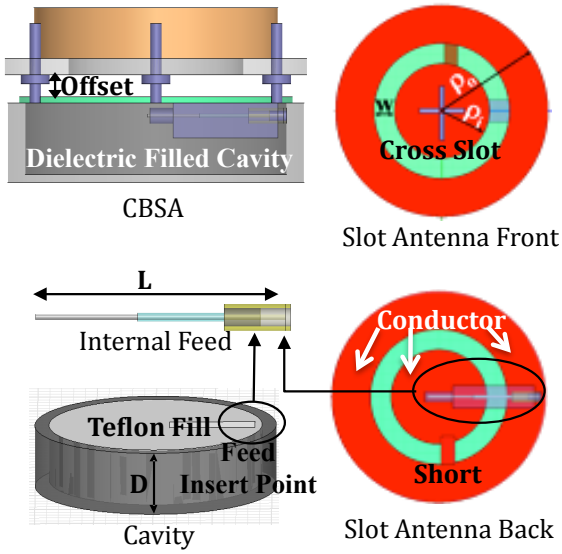

Figure 29. Dimensions of the CBSA.

4.3.2 Simulations

The CBSA was simulated in Ansoft HFSS to validate that the desired antenna characteristics were achieved. The material properties of the Plexiglas specimen holder and Teflon used to fill the cavity were not uniform and varied from sample to sample. As a result, the Plexiglas and Teflon were characterized using the Agilent HP8750 dielectric probe kit, and modeled in HFSS. The antenna was initially designed to operate in free space then redesigned for functionality in close proximity (7 mm) to a skin tissue phantom (ε_r ~44). The skin phantom was also characterized in house and modeled in the simulator.

As illustrated in Figure 30, the various antennas parameters provide design flexibility with regard to size, bandwidth and design frequency. The resonant frequency decreases for increased values of W, ρi, ε_r and ρo. Bandwidth increases for increased values of W, D, and t and decreases as ε_r is increased. In general, the design process

involves configuring these parameters for optimal antenna performance at short distances from the TUI.

Parameter	Variation	Effect	
		BW	f_c
W	Increase	↑	↓
ρ_i	Increase	N/C	↓
ρ_o	Increase	N/C	↓
ε_r	Increase	↓	↓
L	Increase	N/C	↑
D	Increase	↑	↓
t	Increase	↑	↓
	Crossed Slots	↑	N/C

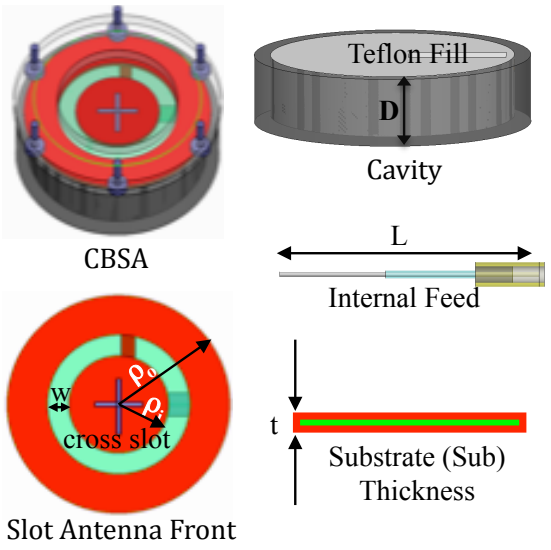

Figure 30. CBSA design parameters and their effect on bandwidth (BW) and design frequency (f_c).

As illustrated in Figure 31 the simulation results prove that the CBSA is broadband (300 MHz), and works well in close proximity to a skin tissue phantom at the design frequency of 1.4 GHz. Simulations also show that the antenna is very efficient (88%), and tunable to ~50 MHz per mm (MHz/mm) of the feed length (Figure 31). The simulated gain and directivity are 3.4 and 3.9 dB, respectively.

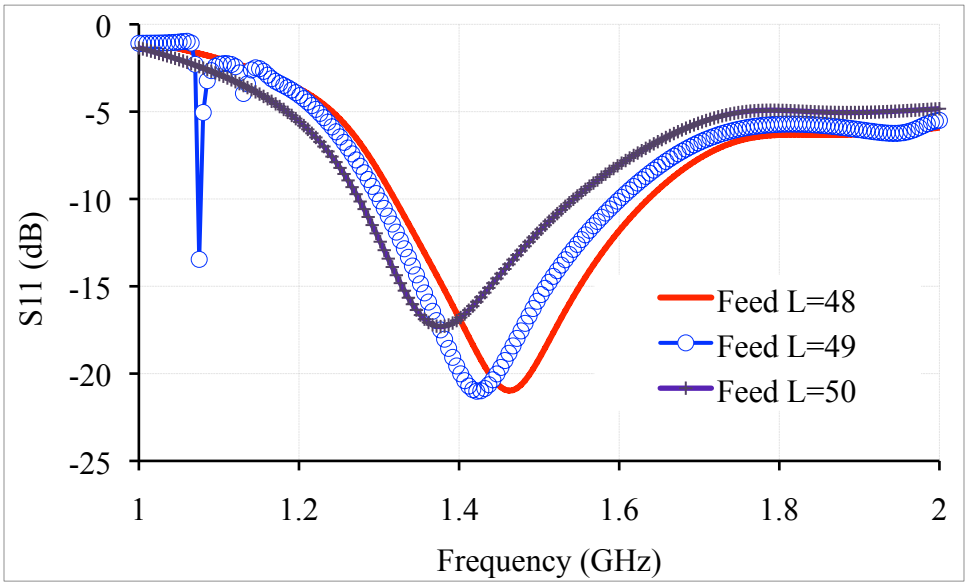

Figure 31. Simulations if S11 in close proximity to a muscle tissue phantom. This figure also shows tunability as a function of feed L: 50 MHz/mm.

4.3.3 Measurements and Human Body Characterization

The CBSA was fabricated and measurements were performed in three conditions: in close proximity to a skin tissue phantom, in free space and in close proximity to a human core. Following are the details of the experiments in each condition.

First the antenna is positioned in close proximity to a skin tissue phantom. The measured and simulated results are comparable. The reflection coefficients at the design frequency (1.4 GHz) are -22 dB and -20 dB for measurements and simulations, respectively. The measured bandwidth is ~400 MHz, which is ~100 MHz wider than that of the simulation (Figure 32). The difference between the measurement and simulation is likely due to the difficulty in fabricating a cavity antenna without boundary discontinuities between the cavity walls and radiating aperture (slot antenna). Previous research has shown that nearly perfect contact is needed between waveguide structures to

avoid boundary condition discontinuities. Whereas the CBSA cavity is analogous to a cylindrical waveguide, any slight discontinuity in the waveguide/cavity walls can produce variations in the surface currents and thus impedance.

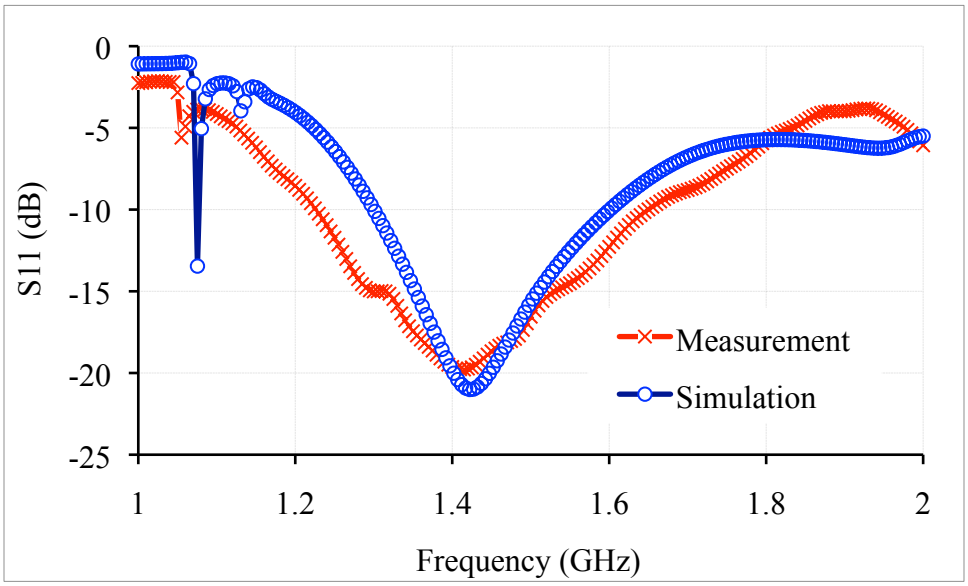

Figure 32. S11: measured versus simulated results with the phantom offset 7 mm from the CBSA.

Second the antenna is characterized while radiating in free space. The measurement results in Figure 33 confirm that directionality was achieved. The measured and simulated radiation pattern results were also comparable. The offset between the antenna and tissue is chosen at the distance in which the worst case degradation occurred in the preliminary study. By analyzing S11 data in Figure 13, it is apparent that the antenna degradation is inversely proportional to the offset distance, with 7 mm being the worst case scenario. Since an acceptable performance can be achieved at larger offset distances, the antenna is designed for optimal performance in the worst case scenario. Therefore the 7 mm offset was chosen for the remainder of this study.

The measurement results in Figure 34 show that at 1.4 GHz the CBSA has a very high reflection when radiating in free space, but when positioned in close proximity to the phantom the reflection is very small, enabling the detection of very low emissions from the TUI, with very low signal loss due to mismatch. This feature could also be used to automatically activate the sensor when brought into a certain distance from the body.

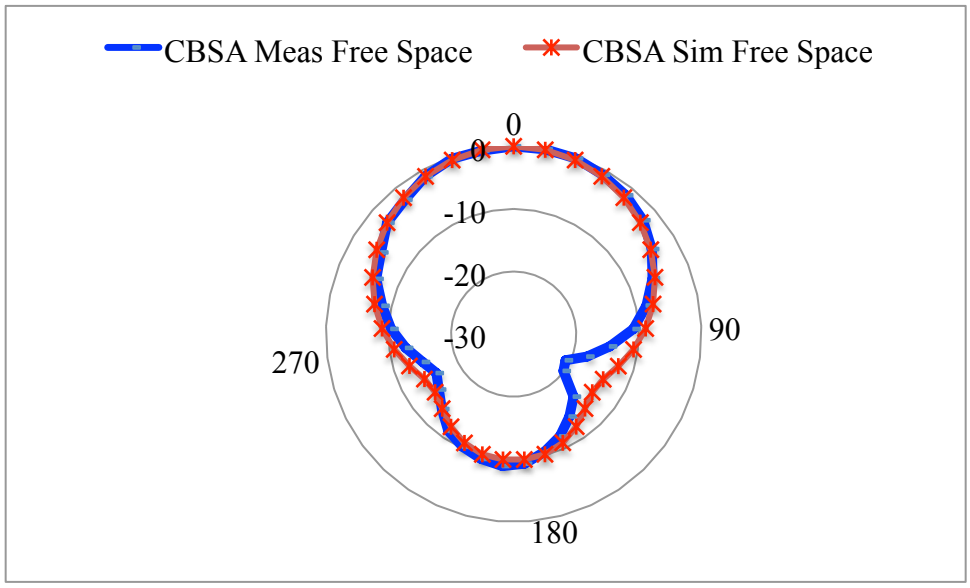

Figure 33. Measured versus simulated normalized radiation pattern of CBSA in dB scale.

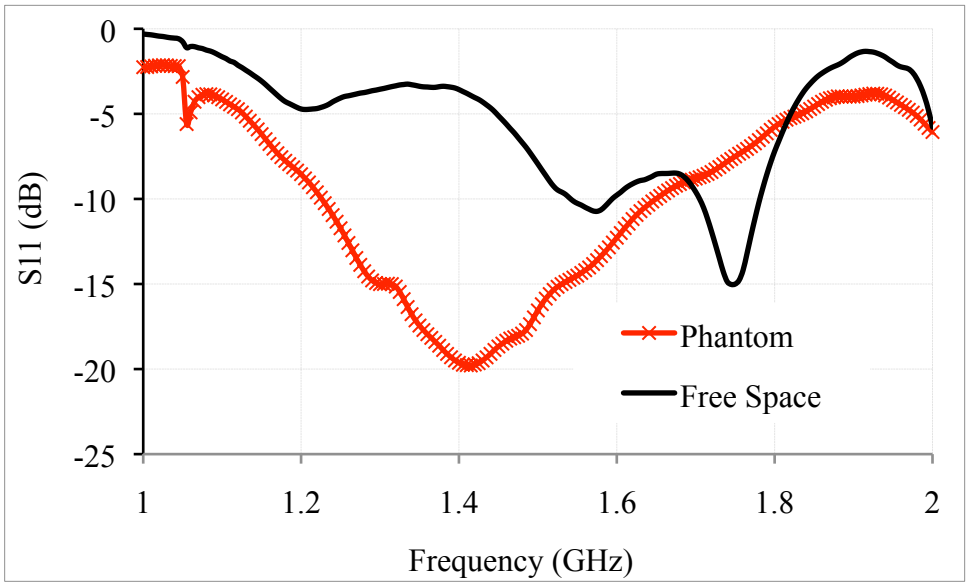

Figure 34. S11 in free space versus phantom with 7 mm offset.

Finally, the antenna was characterized 7 mm from the core of a human subject to verify that the antenna performance holds in practice. Figure 35 shows that the S11 of the antenna in close proximity to the phantom and core of the human subject are virtually identical. This data provides further evidence that the phantom as well as the antenna are well suited for pre-clinical biomedical experimentation.

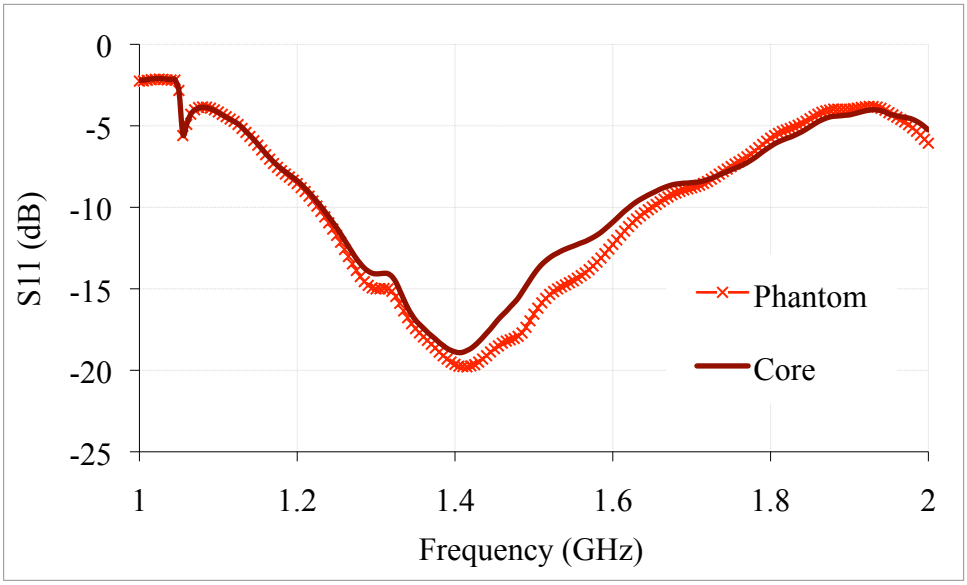

Figure 35. S11: human core versus phantom with 7 mm offset.

4.4 Measurement Test Bed

The measurement test bed is a three layer human core model (HCM) which mimics a conical volume of an abdominal cavity, 50 mm deep with diameters of 55 mm and 75 mm at d = 0 and d = 50 mm, respectively. As illustrated in Figure 36, this volume ideally captures the antenna-sensor main probing region incident to the stomach, which generally takes the form of a Gaussian contour. The HCM is comprised of layered volumes of the solid skin-muscle tissue phantom and liquid blood-fatty tissue phantom previously presented in section 3.5. The ability of the HCM to accurately emulate a human core is demonstrated in the comparison of the electrical properties (Z, ε_r) of the skin, muscle, and blood-fatty tissue phantoms to the Gabriel model. The results were strikingly comparable for each tissue layer; the blood-fatty tissue phantom comparisons are illustrated in Figure 18 – Figure 19, the skin phantom in Figure 22 – Figure 23 and the muscle phantom in Figure 24 – Figure 25.

4.4.1 Rationale for the Human Core Model

The HCM was developed to provide a more concise electromagnetic model of an abdominal cavity than the more commonly used single layer phantoms. Such phantoms are usually developed using simple solid, semi-solid (gels), or liquid solutions [28], [29]. Previous studies have proven that "dielectric layering greatly influences" the radiometric measurement, therefore single layer phantoms cannot accurately mimic the emissive properties of layered volumes human tissue [30]. This loss in accuracy, could create considerable measurement errors, since microwave radiometers detect very low T_B emissions which are dependent on the electrical properties of the tissue.

Liquid phantoms, usually comprised of saline or a water bolus, have a dielectric constant similar to water (~78) at room temperature and 1.4 GHz, whereas human muscle has a dielectric constant of ~54, skin ~44, and fat ~10. As a result the detectable emissions from liquid phantoms will differ from those of human tissue.

Semisolids or gel phantoms have been developed which have similar electrical characteristics to that of skin and muscle tissue, however they are not as durable as solid phantoms. Though semisolids provide a more accurate representation of the body's electrical characteristics across the surface of the TUI, some disadvantages exist when modeling three dimensional volumes of the body's clinical diagnostic regions. For instance thin tissue layers (< 2 mm) such as skin are difficult to develop and manage. Moreover, the versatility of the test bed is reduced, since less dense semisolids may not hold the form factor of the tissue volume, especially at elevated temperatures indicative to that of heat related disorders.

Until this work, no solid skin-muscle phantoms have been developed with electrical properties analogous to human tissue within the 1 – 2 GHz frequency band. There are some single layer phantoms (muscle) which employ an outer shell or cast to hold the form of the TUI. However, the electrical characteristics of the casts, usually plastics, are distinctly dissimilar at the air – skin interface. This interface is the first and therefore critical boundary for extracting subsurface data from the TUI, due to sizable reflections which occur at that boundary which lead to radiometric signal loss. [29] presents a solid 2/3rd muscle phantom which is the currently best available technology for mimicking a human torso. Yet again, this 33% difference in the dielectric constant may present significant measurement errors when extracting deep-seated tissue temperatures using microwave radiometers.

4.4.2 Design of the Human Core Model

The HCM is a durable phantom, designed to mimic the region of diagnosis for core body temperature monitoring, using a layered configuration of the phantoms previously presented in section 3.5. Layers 1 and 2 of the HCM make up the hybrid skin-muscle phantom, comprised of a composite material developed using water and TX-151. The skin layer has a non-uniform thickness, ranging from 1 mm – 2 mm, which is comparable to the combined thickness of the dermis, epidermis, and hypodermis. The muscle layer is located immediately below the skin layer, and also has a non-uniform thickness of 7 mm to 8 mm. Core body temperature is essentially based on the temperature of the circulating blood through the cranial, thoracic and abdominal cavities [31]. Therefore Layer 3, the inner core, is a liquid volume ~40 mm deep which mimics

blood and fatty tissue inside the stomach. The inner core is located inside of a plastic container which with housing to secure the skin-muscle phantom approximately 1 mm in thickness. Since the radiometer detects thermal emissions across the depth of the tissue, the effect of the container is negligible, being that it's a thin, highly emissive material, located beneath the critical air-skin interface. Herein, extreme body temperature changes are simulated by varying the temperature of the inner core to temperatures representative of heat related disorders.

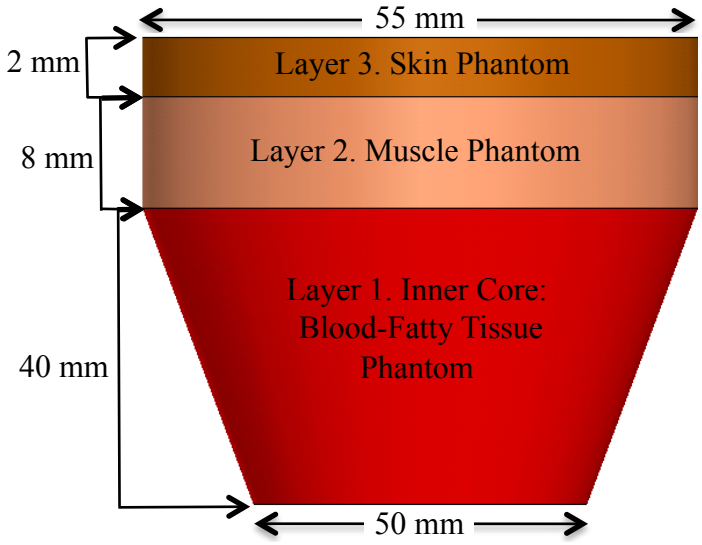

Figure 36. The human core model (HCM).

4.5 Experimentation

As illustrated in Figure 37, the measurement test bed is analogous to the experimental setup presented in the preliminary study, except the skin-muscle phantom is added to complete the human core model (HCM). Although the second generation design incorporates various enhancements to the test bed, the experimental procedure remained consistent with the 1st generation design, to provide an exact performance

comparison and demonstrate the repeatability of the measurement. The measurements were performed with the HCM positioned approximately 7 mm from the antenna. In an effort to mimic changes in core body temperature; the temperature of the skin and muscle phantom layers were kept constant, as the temperature of the core was varied just outside the dynamic range of extreme body temperatures; 107 °F – 92 °F: Human body temperatures in the range of 92 °F to 100 °F are considered normal. Temperatures outside this range are considered adverse with $T < 92$ °F being hyperthermic, and $T \geq 100$ °F exhaustion or heat stroke [25].

The physical temperature of the skin phantom was tracked using a thermocouple placed on the surface. The inner core was tracked using an average temperature from three evenly spaced internal thermocouples positioned at a depth of ~35 mm beneath the skin layer and ~22 mm beneath the muscle layer. The brightness temperature of the HCP was tracked using the radiometer and the raw data was processed via the NCM [32]. The post processed NCM results are presented in section 5.2.1 along with a sensitivity analysis in the section 5.2.2.

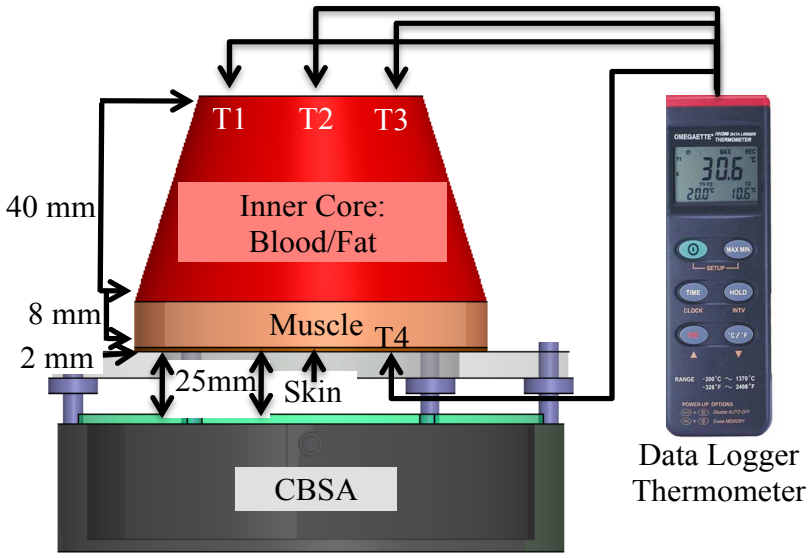

Figure 37. 2nd generation measurement test bed.

4.6 Conclusion

This chapter presents the 2nd generation design, which consists of a modified sensor design and enhanced antenna to circumvent obstructive phenomena which typically occur in the near field of the body. Device miniaturization and continuous calibration allows for improved stability, accuracy, and resolution without the need for additional automatic gain control circuitry. The D – C I/Q architecture enables device miniaturization by means of smaller components. In turn, thermal stability is easier to implement on devices with a smaller form factor. A multiport RF switch is added for continuous calibration which generates a calibration curve for each measurement interval. To facilitate optimal performance of the sensor at short distances from the TUI, a CBSA is designed to compensate for impedance mismatch, bandwidth degradation, and other near field effects previously demonstrated in the preliminary study. Table 8 demonstrates the antenna performance enhancements as compared to the 1st generation design. These

performance specifications were selected are based on the antenna requirements for biomedical applications, presented in section 3.3. This chapter also presents an enhanced measurement test bed, which has been modified from a discrete to multi-layer human core model (HCM) that mimics a three dimensional volume of an abdominal cavity. The results from experimentation and testing of the MRBS on the HCM is presented in section 5.2.1.

Table 8. PD1 versus CBSA performance characteristics.

Parameter	PD1	CBSA
Resonant Frequency (GHz)	1.45	1.41
Gain (dB)	1.56	3.4
Directivity (dB)	2.45	3.9
Efficiency (unit less)	0.85	0.88
Near-Field Bandwidth (MHz)	150	400

CHAPTER 5

THE NON-CONTACT MODEL

This chapter provides a comprehensive investigation to first identify then isolate the artifacts that obstruct the near field measurement. Although proper antenna design and offset distance can mitigate antenna-body effects towards subsurface temperature *tracking,* the preliminary study (presented in section CHAPTER 3), as well as [10] – [12] provide evidence that simply minimizing near field effects is inadequate for absolute temperature extraction. This is mainly due to the fact that the detectable energy emitted from deep – seated tissue is yet quite difficult to extract due to various reasons: 1) thermal emissions at microwave frequencies are very low, on the order of 10^{-14} watts; 2) these substantially faint signal levels are slightly larger than the ambient temperature noise floor, and are extracted from a potentially noisy environment; 3) in addition to 1) – 2), the detectable energy is attenuated considerably upon reaching the input of the receiver due certain artifacts which arise as a result of the non contacting nature of the sensor: Imperfections in the antenna design, and sizeable signal loss at the air – skin interface are the most critical.

Therefore a Non-Contact Model (NCM) is derived which correlates the observed brightness temperature to the subsurface temperature which accounts for 3), since the sensor itself is designed to compensate for 1) – 2). Thereafter the radiometric data extracted from experimentation in section 4.5 is processed through the NCM and a

sensitivity analysis is presented to determine the degree to which non-contacting artifacts effect and or degrade the measurement.

5.1 Derivation

The Non-Contact Model (NCM) presented herein provides a mathematical formulation to account for artifacts that arise from the sensor's remote positioning from the TUI. The parameters which affect the measurement are first identified and then conjugated to derive the NCM. Though similar parameters have been presented in [33] from a far-field remote sensing perspective, in this work the NCM parameters are defined in the context of near field radiometric sensing.

Figure 38 illustrates the three stages of the NCM derivation presented in this section:

1) *Measurement of Brightness Temperature,* T''_{SKN}
2) *Correction at the Antenna Interface,* T'_{SKN}
3) *Correction at the Air-TUI Interface,* T_{SKN}

T_{SKN} is the final output of the non-contact model and represents the subsurface temperature across the depth, extracted at a point just below the surface of the skin.

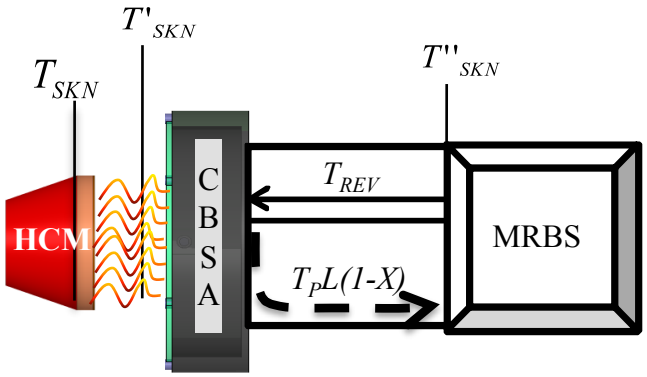

Figure 38. Stages of the NCM.

5.1.1 Stage 1 – Measurement of the Brightness Temperature

Before applying the NCM, the specimen brightness temperature (T''_{SKN}) is extracted from the measurement via calibration, which relates the input T''_{SKN} to the output indicator (voltage, power, current), where T''_{SYS} is the total noise contribution delivered to the system before the NCM correction. In our case the voltage output is correlated to an absolute temperature from the physical temperatures of the calibration loads inside the radiometer.

$$T''_{SKN} = T_{SYS} \tag{8}$$

5.1.2 Stage 2 – Correction at the Antenna Interface

The antenna is the primary sensing mechanism for non-invasive extraction of biological data from the TUI, thus a complete understanding of the antenna parameters is of critical importance to obtaining an accurate measurement. Due to the close, non-contact positioning of the sensor and the TUI, the antenna parameters presented are characterized from a close proximity perspective.

The antenna efficiency (η_e), physical temperature of the antenna (T_p) and the antenna transmission efficiency due to the impedance match (X), mutually affect the signal (biological data) detected by the antenna. An antenna with a low efficiency attenuates the detected signal by a factor of η_e. As discussed in Chapter 2, thermal conduction from the TUI heightens (T_p), in close proximity sensing applications. X is derived by first integrating the near field reflection coefficient ($\Gamma_{A\text{-}I}$) across the antenna bandwidth *B*, where Δf and *df* denote the frequency step of the integral (9). Ideally the antenna is designed such that the 10 dB return loss bandwidth encompasses the frequency band of the radiometer as determined by its internal filtering. Transmission is denoted as one minus the reflection; accordingly the formula for X is presented in (9).

$$X = 1 - \int_B \left|\Gamma_{A-I}\right|^2 df = 1 - \frac{\sum \Delta f \left|\Gamma_{A-I}\right|^2}{B} \qquad (9)$$

The combination of suboptimal antenna efficiency and impedance mismatch attenuates the detected signal. Moreover, antenna-TUI thermal conduction, results in the generation of thermal noise which propagates through the system and distorts the T''_{SKN} measurement. These phenomena are modeled in (10), where $T'_{SKN\text{-}1}$ is the first step in the T'_{SKN} derivation.

$$T'_{SKN-1} = \frac{T_{SYS} - T_p(1-\eta_e)X}{\eta_e X} \qquad (10)$$

From the antenna-body near field the specimen brightness temperature is extracted via the main probing footprint, illustrated in Figure 39, which is equivalent to the antenna main lobe in the far field. This region also defines the spatial resolution of the sensor. An antenna with a perfect broadside radiation is unrealizable. Therefore some ambient temperature contributions from the secondary probing hemisphere (T_{SL})

will affect the measurement. η_{ml} and η_{sl} represent the efficiency of the main probing footprint and secondary probing hemisphere, respectively. η_{ml} is calculated through normalization of the antenna main beam efficiency resolved to its near field component, a similar approach is employed by near field ranges to resolve the far field radiation pattern; a review of the theory is presented in [34]. The relationship between η_{ml} and η_{sl} is provided in (11).

$$\eta_{sl} = 1 - \eta_{ml} \quad (11)$$

By combining equations (8) - (11)the derivation incorporating all of the antenna parameters is presented in (12), where T'_{SKN-2} is the second step in the T'_{SKN} derivation.

$$T'_{SKN-2} = \frac{T'_{SKN-1} - T_{SL}(1-\eta_{ml})}{\eta_{ml}} \quad (12)$$

As illustrated in Figure 38, noise emanating from the input of the radiometer receiver in the direction of the antenna (T_{REV}) is a function of the transmission loss (L) in the signal path between the antenna and radiometer. T_{REV} can be mitigated by integrating an isolator in the radiometer-antenna transmission path. The noise temperature that is then reflected back into the system input is denoted by T'_{REV} in (13), where T_{PI} is the physical temperature of the component at the reflection interface (in this case an isolator termination).

$$T'_{REV} = T_{pI} L(1-X) \quad (13)$$

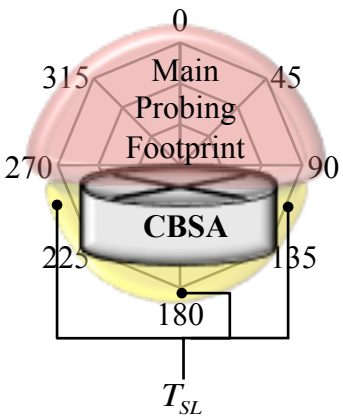

Figure 39. Antenna near field main primary probing footprint ($90 \leq \theta$, $\theta \geq 270$) and secondary probing hemisphere ($90 < \theta < 270$) in the elevation (θ) plane.

The final derivation of the stage 2 NCM, incorporating the antenna interface correction and T'_{REV} is presented in (14) and Figure 40.

$$T'_{SKN} = T'_{SKN-2} - T'_{REV} = \frac{T_{SYS} - T'_{REV} - T_{SL}(1-\eta_{ml})\eta_e X - T_p(1-\eta_e)X}{\eta_e \eta_{ml} X} \quad (14)$$

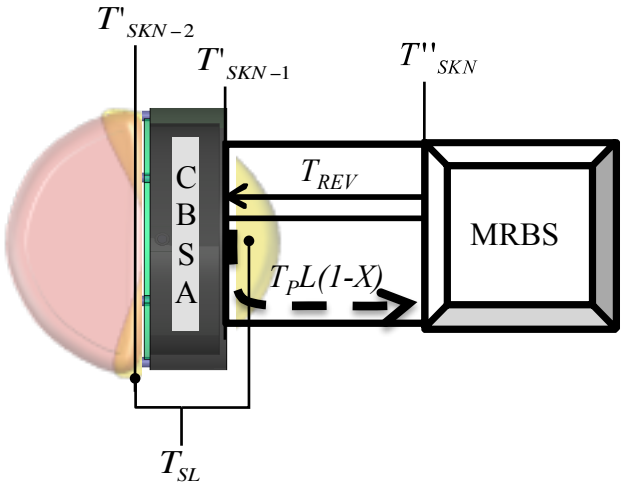

Figure 40. Corrections at the antenna interface.

5.1.3 Stage 3 – Correction at the Air-TUI Interface

Stage 3 of the NCM accounts for the effects of the specimen emissivity denoted by *e*. The product of *e* with the physical temperature yields the specimen brightness temperature. As described in [35] the input impedance of the antenna (50 Ω) is usually well matched to the human body (~59Ω) at radio frequencies. Thus, when the antenna is placed in direct body contact electromagnetic (EM) waves are coupled through the antenna-body boundary with negligible interference. In non-contact sensing applications EM propagation becomes non-trivial due to impedance discontinuities across the air-TUI boundary. Human tissue typically has a very high relative permittivity ε_r, with the lowest being fat (ε_r = ~9) and the highest being blood (ε_r = ~59). When a material with a high dielectric constant is bounded by air, sizeable reflections are introduced. As a result weak EM emissions from the TUI are attenuated by a factor of 40% - 60% at RF frequencies. This phenomenon significantly heightens the difficulty in attaining an absolute subsurface temperature measurement.

Herein the emissivity of the TUI is represented by (15) and is related to the ε_r of the specimen by (16). The air-skin reflection is defined by $R_{A\text{-}S}$, with ε_r denoting the relative permittivity of the specimen.

$$e = 1 - \left|R_{A-S}\right|^2 \tag{15}$$

$$R_{A-S} = \left|\frac{1-\sqrt{\varepsilon_r}}{1+\sqrt{\varepsilon_r}}\right| \tag{16}$$

While the strong impedance mismatch at the air-TUI interface attenuates the emissions from the TUI, it has the effect of intensifying the ambient atmospheric contributions

(T_{DN}). Accordingly, *e*, $R_{A\text{-}S}$, X, η_{ml} and η_e also impact the effect of T_{DN}. The complete NCM is presented in (17)

$$T_{SKN} = \frac{T_{SYS} - T'_{REV} - T_{SL}(1-\eta_{ml})\eta_e X - T_p(1-\eta_e)X - T_{DN}X\eta_{ml}\eta_e(1-e)}{\eta_e\eta_{ml}Xe} \qquad (17)$$

5.2 Implementation

The NCM was applied to radiometric data extracted from measurements performed on the enhanced test bed (discussed in section 4.4 – 4.5), to emulate subsurface temporal monitoring. The accuracy of the NCM is validated first, through an analysis of the measurement data extracted from the test bed before and after being processed through the model. These results demonstrate a substantial improvement in accuracy after applying the NCM. Thereafter, a sensitivity analysis is performed to show the sensitivity of the measurement to the model parameters.

5.2.1 Data and Results

In Figure 41 the extracted temperature profile of T_{SKN} is compared with the physical temperatures of the skin and core. These results show that T_{SKN} follows the thermal profile of the inner core, which is very different from the thermal profile of the skin surface. Also illustrated in Figure 41 is the degree to which the accuracy of the measurement is improved following application of each stage of the NCM. T''_{SKN} follows the thermal trend of the inner core more precisely than that of the skin layer but with minimal accuracy. As enhancements are added to the model, the correlation to the inner core temperature improves with T'_{SKN}, and T_{SKN} provides the optimal response.

Figure 42 shows the absolute percent difference between the physical temperature of the core and the extracted temperatures from each stage of the NCM. As the temperature of the core decreases as a function of time, thermal energy is conducted through muscle and skin layers, which heightens the emissions from the intervening layers. In essence, the radiated emissions across the tissue depth are heightened at the T'_{SKN}, and T_{SKN} interfaces. As a result the percent difference between the core, T'_{SKN}, and T_{SKN} seem to decrease as a function of time, as illustrated in Figure 42. The highest percent difference between T_{SKN} and the core is 8%, and this value will be considered as a reasonable percent difference threshold for the sensitivity analysis that follows in section 5.2.2.

The results in Figure 41 and Figure 42 also reveal that T_{SKN} is lower than the physical temperature of the inner core. This result is expected and is due to the fact that wave propagation through the HCM layers is attenuated and non-coherent, resulting in reflections and signal loss from layer to layer. As a result the percent difference between the physical and radiometric measurements are fairly high. A direct correlation between the detected brightness temperature and the inner core temperature requires the additional step of incorporating the propagation effects of the HCM into the extraction process, which is demonstrated in the chapter following.

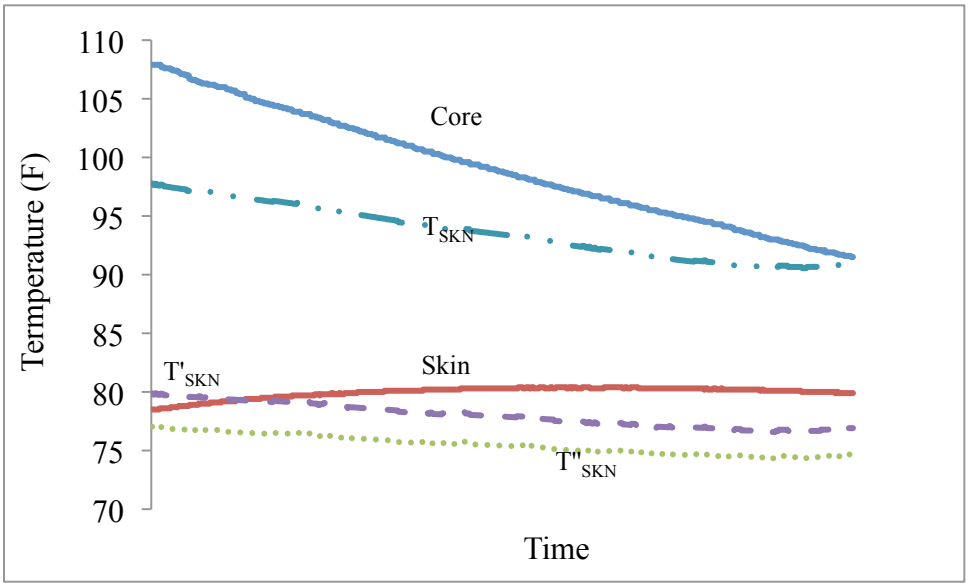

Figure 41. Physically measured temperatures of skin and core model (dashed lines) and brightness temperature measurements (solid lines) before (T''$_{SKN}$) and after applying the NCM (T'$_{SKN}$, T$_{SKN}$).

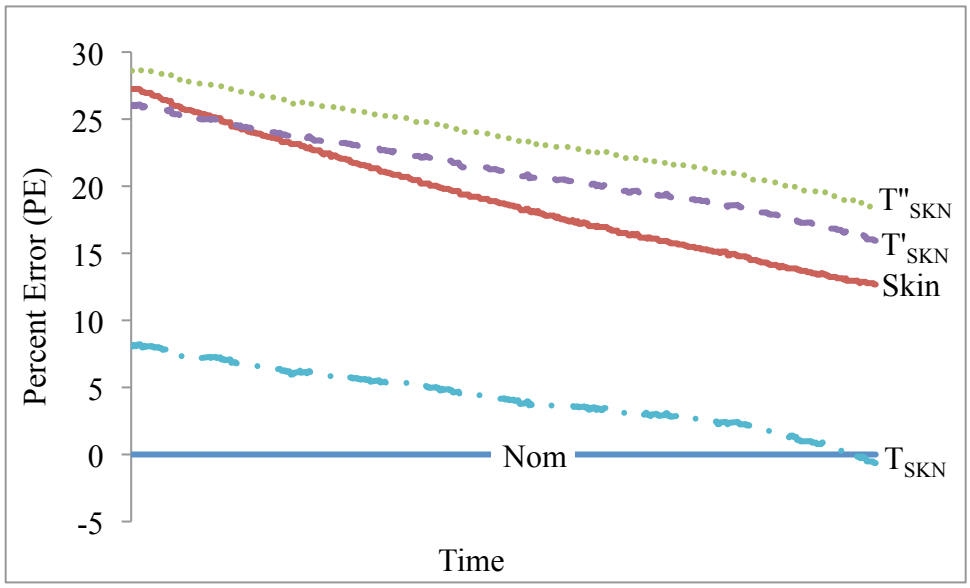

Figure 42. Absolute, percent difference between the core temperature (Nom), skin surface (Skin) and radiometer measurements before (T''$_{SKN}$) and after (T'$_{SKN}$, T$_{SKN}$) applying the NCM.

5.2.2 Sensitivity Analysis of the NCM Parameters

A sensitivity analysis was performed to determine the model parameters to which the measurement is most sensitive, which would in turn identify the parameters which require more precise characterization and monitoring. The nominal value of each parameter is assumed to provide the optimal T_{SKN} response. The analysis is performed via percent error plots of T_{SKN} as the NCM parameters are varied from their nominal values within ranges that would be realizable in practice. Certain parameters cause a change in the T_{SKN} response over time therefore the analysis is performed in 15 minute intervals with "start" denoting the point in the measurement at which the core temperature is 107 ºF.

Figure 43 demonstrates that if X is slightly degraded to 0.9 from 0.957 the percent error would be 12%, which is much greater than the 8% threshold. This result is noteworthy because the characteristics of most antennas vary when in close proximity to biological media. In practice, X could degrade to well below 0.9. An accurate measurement was achieved in this work by designing the antenna for optimum functionality in close proximity to the TUI, therefore minimizing input match reflections. As shown in Figure 44, the measurement is also quite sensitive to T_{DN}. A ±5% variation from the nominal T_{DN} value of 65 ºF (ambient temperature), induces error percentages of ±36%, which is also well beyond the threshold. This is attributed to the fact that sizable contributions of T_{DN} are reflected across the tissue into the sensor, contrary to on-body radiometric sensors which have no reflected T_{DN} contribution due to the sensor being in direct contact with the TUI. In practice T_{DN} varies with the temperature of the space suit and therefore must be known to a high degree of accuracy. Implied by equations (15) –

(17), this T_{DN} reflection phenomenon has the greatest effect on media with a high dielectric constant such as skin tissue.

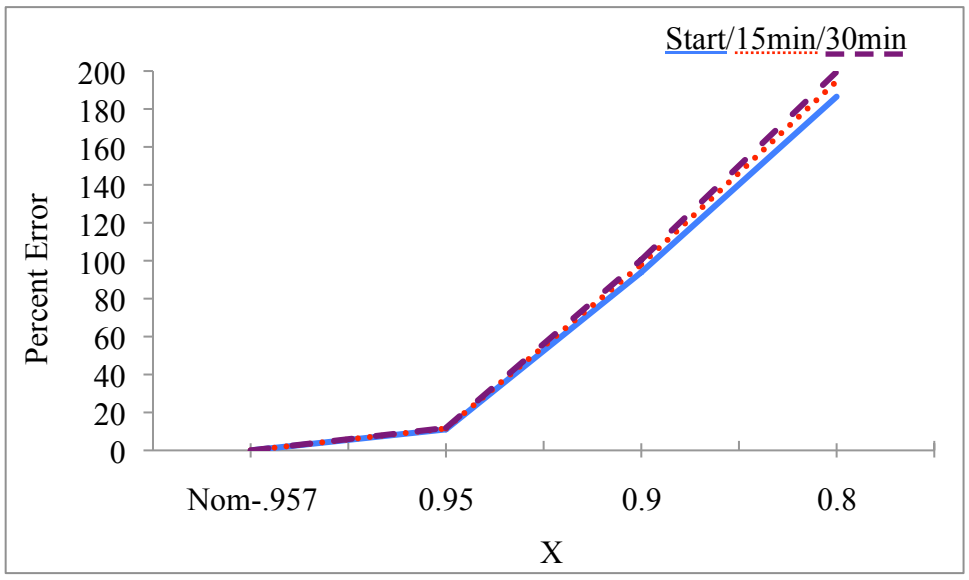

Figure 43. Percent error in the T_{SKN} measurement taken at 15 minute intervals as X is varied from the nominal value (Nom) of 0.957.

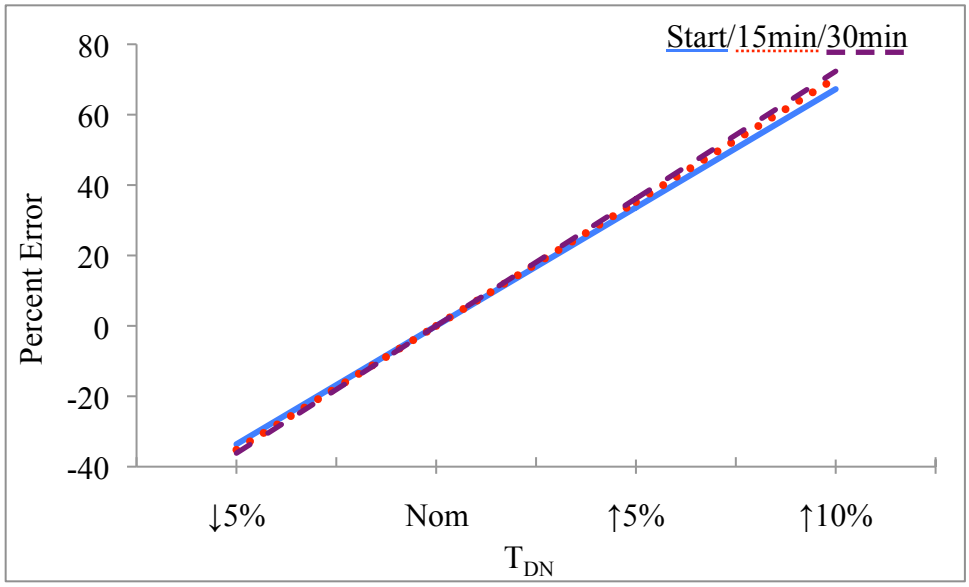

Figure 44. 12 Percent error in the T_{SKN} measurement taken at 15 minute intervals as T_{DN} is varied from the nominal value (Nom) of 65 ºF.

The measurement is least sensitive to T_p, *e*, η_e, η_{ml} and especially T_{SL} (see Figure 45) which further justifies the close proximity approach and enables design flexibility. For instance, section 2.1 references previous works which describe placement issues associated with the on-body approach that distort the measurement such as thermal conduction between the specimen and T_P. Figure 46 provides evidence that the close proximity measurement is not very sensitive to T_P. However, this parameter should be known with good accuracy, since the percent error increases beyond the desired 8% threshold as T_P is varied by ±5%. Figure 47 illustrates that the measurement is least sensitive to *e*, and the percent error varies with respect to time. This data implies that variations in *e* from person to person will have minimal effect on the accuracy of the close-proximity measurement. The same analysis was performed on η_e and η_{ml} and the percent error results were virtually identical – there was a small variation in T_{SKN}

measurement over time and the 8% error thresholds occurred around 0.6, whereas the nominal values are 0.88 and 0.95, respectively, Figure 48.

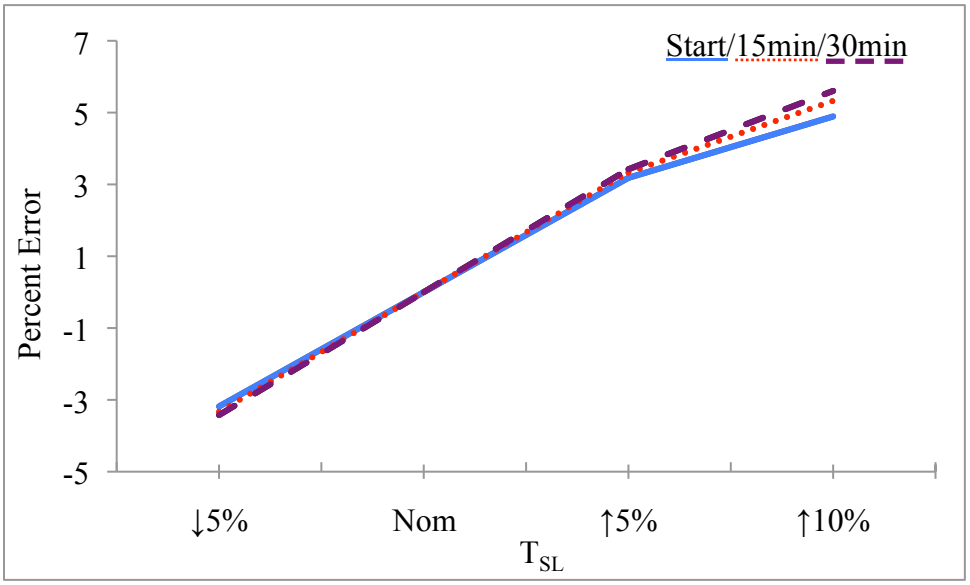

Figure 45. Percent error in the T_{SKN} measurement taken at 15 minute intervals as T_{SL} is varied from the nominal value (Nom) of 65 ºF.

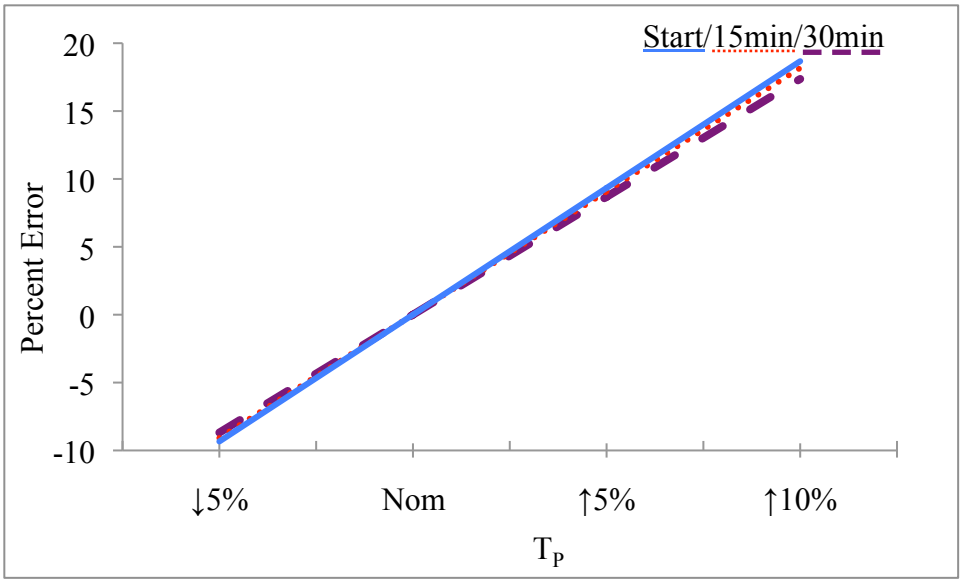

Figure 46. Percent error in the T_{SKN} measurement taken at 15 minute intervals as T_P is varied from the nominal value (Nom) of 65 ºK.

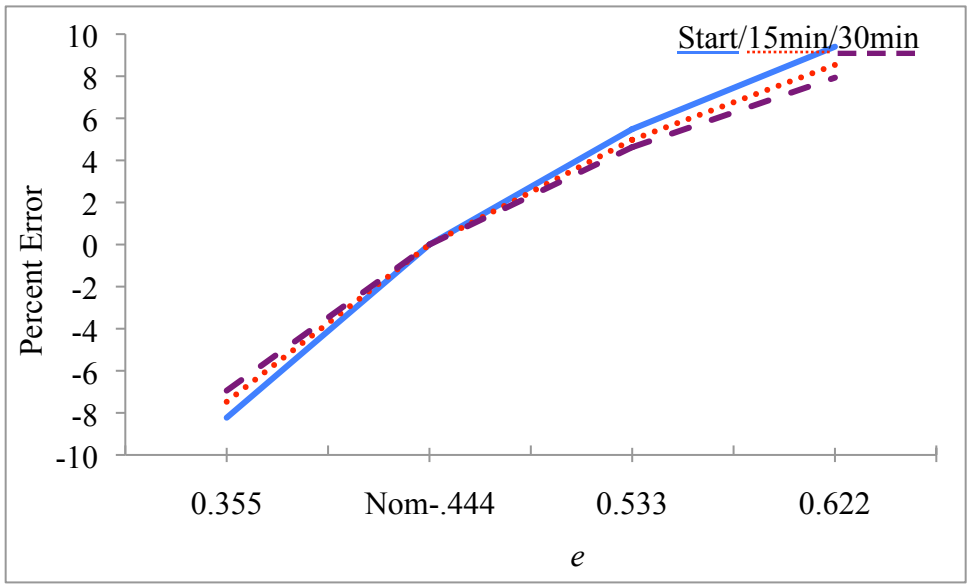

Figure 47. Percent error in the T_{SKN} measurement taken at 15 minute intervals as *e* is varied from the nominal value (Nom) of 0.444.

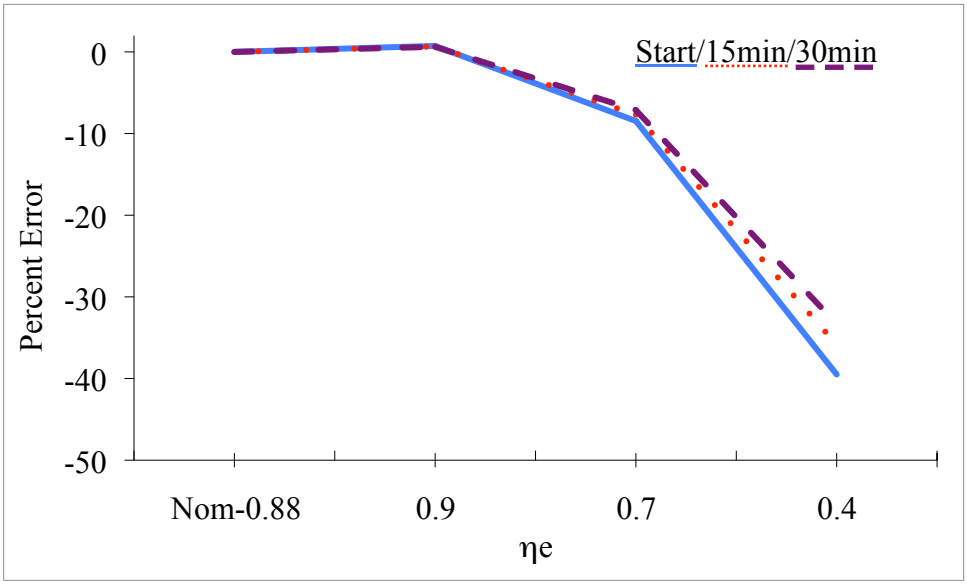

Figure 48. Percent error in the T_{SKN} measurement taken at 15 minute intervals as ηe is varied from the nominal value (Nom) of 0.88.

5.3 Conclusion

A mathematical representation in the form of a non-contact model was derived and implemented on data extracted from close proximity measurements performed on the HCM. The correlation between the physical temperature of the inner core of the human phantom and the extracted subsurface temperature was within 8% difference. In CHAPTER 6 further enhancements are achieved by implementing a model to account for propagation effects throughout the phantom.

A sensitivity analysis was performed to determine which model parameters the measurement is most sensitive to. This work provides evidence that the measurement is most sensitive to atmospheric contributions and antenna impedance match, the latter being influenced by the presence of biological media. The close proximity measurement is less sensitive to the physical temperature of the antenna, which has been known to distort on-body measurements. Moreover minimal sensitivity to the antenna efficiency

and main probing hemisphere enables antenna design flexibility. The measurement is least sensitive to the emissivity of the specimen, which implies that the MRBS performance will have minimal variation from person to person.

CHAPTER 6

TISSUE PROPAGATION MODEL (TPM)

This chapter presents a mathematical model for incoherent propagation of thermal radiation throughout the human body. The model is developed to complement subsurface body temperature measurements made using the MRBS, and processed through the NCM. The data presented in this chapter was aggregated from the experiment in section 4.5. The NCM was applied to the experimental data and the results presented in section 5.2.1. In this chapter, the post-processed NCM data is yet again processed through the TPM, which further improves the accuracy towards an absolute core body temperature measurement. The core body temperature extraction process is presented in section 6.4.

6.1 Rationale for the TPM

Microwave radiometers detect the brightness temperature of the specimen across the sensing depth, which is dependent on the electrical properties of the intervening tissue layers. For this reason, previous studies have demonstrated that "dielectric layering greatly influences" the radiometric measurement [30]. In the context of electromagnetic wave propagation, the human body is characterized as a lossy medium, comprised of stratified tissue with dissimilar permittivity values. These characteristics heighten the complexity of extracting subsurface physiological data from the body. As electromagnetic waves propagate through the body, a portion of the power is dissipated

due to the lossy nature of the tissue. The isotropically-propagating energy is further attenuated by dielectric mismatch which gives rise to reflections at the tissue boundaries. As a result, thermal emissions radiated from deep within the body have only a marginal effect on the brightness temperature at the skin surface, making it very difficult to monitor changes in core body temperature without considering the electrical properties of the blood and muscle tissue. Supporting data has been presented in physiological studies which provides evidence that the skin surface temperature alone does not provide an accurate estimate of core body temperature even with correction [8]. In fact, thermal variations on the order of ±7 ºF from homeostasis, 98 ºF, will only result in a change in skin temperature of ±1 ºF. Here the need for a non-invasive measurement method becomes apparent.

In section 4.5, subsurface temperature variations of the HCM were tracked using the MRBS without considering a priori knowledge of the electrical properties of the internal tissue, i.e. muscle and blood-fat. Only the dielectric properties of the skin surface were considered in the analysis. After applying the NCM, an acceptable percent difference of 1.2% - 8% was achieved between the physical temperature measured internally using thermal probes, and the radiometric brightness temperature, even though the emissive properties of the deep-seated tissue were not considered (see Figure 42 in section 5.2.1). Nevertheless, the accuracy of the measurement can be improved by taking the electromagnetic properties of the subcutaneous tissue into account. Moreover, the percent difference between the brightness temperature and physical temperature should be minimal, well below 3 °F (3%), since small deviations in core body temperature are

used in the diagnosis of heat related disorders [25], and as a pre-clinical diagnostic tool for disease and other health related abnormalities.

For instance, thermal homeostasis of the human body is maintained from 98 °F to 100 ºF. Heat exhaustion and stroke are diagnosed at temperatures above 104 °F, which is only ~6% above homeostasis. Moderate to severe hypothermia is diagnosed below 90 ºF, or 9% below homeostasis. Therefore the percent difference values achieved using only the NCM are unacceptable for true core body sensor. Hence, the goal of this work is to improve the accuracy of the close proximity radiometric sensing modality to a percent difference value well below 2% by introducing a mathematical formulation to model radiative transfer through the human body.

6.2 The TPM Derivation

The tissue propagation model (TPM) depicts radiative transfer through three tissue layers of an abdominal cavity compromised of skin, muscle, and blood-fatty tissue. Accordingly, the TPM derivation is applied to the HCM, with the tissue defined as stratified lossy dielectrics. Coherent transmission effects and angular dependence is ignored in the TPM since scattering will be negligible at the air-skin boundary which is spatially homogeneous, given that the wavelength of the sensing frequency of 1.4 GHz (λ = 230 mm) is much larger than the roughness of the tissue under investigation TUI [36], keratinocyte skin cells with size and roughness on the order of micrometers. Therefore, in our case the more complicated coherent approach, will yield results very similar to that of the incoherent approach, as demonstrated in the final analysis. It has also been proven that the angular dependence is negligible in media with a high dielectric constant [36]

such as human tissue, since the polarization of the waves emanating from the tissue will remain relatively normal to the respective boundary or transmission interface. Moreover, the radiated signal is expected to be co-polarized with the observation angle of the sensor, assuming the device remains relatively parallel with the TUI inside the uniform of servicemen.

The TPM derivation is based on Ulaby's equations for apparent brightness temperature of a terrain with a nonuniform dielectric profile in [36]. These equations have been correlated to the HCM, except the reflection at the muscle-blood boundary is ignored since the dielectric contrast between muscle and blood-fatty tissue layers is minimal.

The TPM derivation is implemented in four levels:

1) *Definition of the Individual Strata (tissue layer) Emissions,* $T_{s.t}$
2) *Derivation of the Up and Down-Welling Emissions per Layer,* $T_{t.U}$ *and* $T_{t.D}$
3) *Derivation of the Net Apparent Emissions from all Stratum,* T_B
4) *Derivation of Apparent Brightness Emissions,* $T_{AP.B}$

A graphical representation of the TPM is presented below in Figure 49.

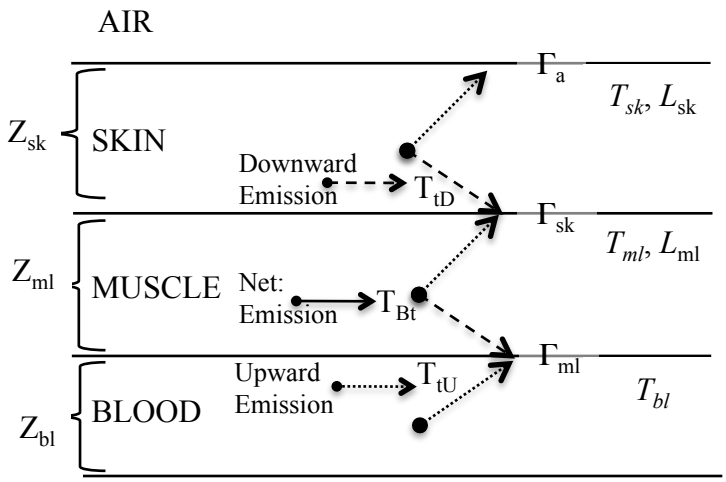

Figure 49. Graphical representation of the TPM.

6.2.1 Definition of the Individual Strata Emissions

To begin, the strata temperatures $T_{s.t}$ are defined, which are the total transmitted emissions (before reflections) at each tissue layer, with t representing the tissue layer itself: t = a – air , t = sk – skin , t = ml – muscle , and t = bl – blood. The expressions for $T_{s.t}$ are provided in (18) – (20), wherein L_t is the loss in the tissue and T_t is the physical temperature of the strata. The formula for the loss contributions in each layer (L_t), is presented in (21) where α_t is the attenuation constant (22), δ_t is the thickness of the tissue layer, $\varepsilon_{r,t}$'' is the imaginary part of the dielectric constant and $\varepsilon_{r,t}$' the real part, per layer.

$$T_{s.bl} = T_{bl} \tag{18}$$

$$T_{s.ml} = T_{ml}\left(1 - \frac{1}{L_{ml}}\right) \tag{19}$$

$$T_{s.sk} = T_{sk}\left(1 - \frac{1}{L_{sk}}\right) \tag{20}$$

$$L_t = e^{\alpha_t \delta_t} \tag{21}$$

$$\alpha = \omega \sqrt{\left[\frac{\mu \varepsilon_{r,t}' \varepsilon_0}{2} \left(\sqrt{1 + \left(\frac{\varepsilon_{r,t}''}{\varepsilon_{r,t}'} \right)^2} \right) - 1 \right]} \tag{22}$$

6.2.2 Derivation of the Up and Down-Welling Emissions per Layer

To derive an expression for the up and down-welling contributions per layer, a similar procedure is followed to that of [36], wherein a binomial expansion $(1-\chi)^{-1}$ is formed from a derived expression which takes into account all reflections and losses throughout the stratified tissue. The formula for χ is presented in (23). In this case, χ accounts for losses and reflections between the air – skin and muscle – blood boundaries, while discarding the negligible reflections at the skin – muscle boundary. The closed form of the binomial series is multiplied by an additional $(1-\Gamma_a)$ to account for transmission at the air – skin interface. We define this closed form expression as the coefficient of multiple reflections (CMR) in (24), where Γ_t is the reflection coefficient at the tissue boundary as illustrated in Figure 49. The CMR is used in the derivation of the individual up and or down-welling temperature contributions in each layer. Thus, the up-welling contribution for the blood-fatty tissue layer is presented in (25), while the up and down-welling contributions for the muscle and skin strata are defined in (26) – (27), and (28) – (29), respectively.

$$\chi = \frac{\Gamma_{ml}\Gamma_a}{\left(L_{ml}L_{sk}\right)^2} \quad (23)$$

$$CMR = \frac{\left(1-\Gamma_a\right)}{1-\frac{\Gamma_{ml}\Gamma_a}{\left(L_{ml}L_{sk}\right)^2}} \quad (24)$$

$$T_{bl.U} = T_{s.bl}\left(\frac{1-\Gamma_{ml}}{L_{ml}L_{sk}}\right)\left[CMR\right] \quad (25)$$

$$T_{ml.U} = \left(\frac{T_{s.ml}}{L_{sk}}\right)\left[CMR\right] \quad (26)$$

$$T_{ml.D} = T_{s.ml}\left(\frac{\Gamma_{ml}}{L_{ml}L_{sk}}\right)\left[CMR\right] \quad (27)$$

$$T_{sk.U} = T_{sk}\left(1-\frac{1}{L_{sk}}\right)\left[CMR\right] \quad (28)$$

$$T_{sk.D} = T_{s.sk}\left(\frac{\Gamma_{ml}}{L_{ml}^{\ 2}L_{sk}}\right)\left[CMR\right] \quad (29)$$

6.2.3 Derivation of the Net Apparent Emissions from all Stratum

The net apparent brightness emissions from all stratum (T_B) is comprised of the up and or down-welling emissions per layer, while taking all reflections into account. The total up and down-welling contributions for each individual layer is represented by $T_{B.t}$ in (30) – (32). As illustrated in Figure 49, $T_{B.bl}$ acts as a source, due to its assumed infinite thickness, and only has an upwelling temperature contribution $T_{bl.U}$ (30). Infinite thickness is assumed in $T_{B.bl}$ since the depth of the blood-fatty tissue layer goes beyond that of the sensor penetration depth. $T_{B.ml}$ and $T_{B.sk}$ are comprised of up-welling emissions T_{tU} as well as down-welling emissions T_{tD}. These expression are provided in

(31) – (32). Hence, T_B is effectively the sum of the net apparent emissions from all three layers (33).

$$T_{B.bl} = T_{bl.U} \quad (30)$$

$$T_{B.ml} = T_{ml.U} + T_{ml.D} \quad (31)$$

$$T_{B.sk} = T_{sk.U} + T_{sk.D} \quad (32)$$

$$T_B = T_{B.bl} + T_{B.sk} + T_{B.ml} \quad (33)$$

6.2.4 Derivation of Apparent Brightness Emissions

The ultimate goal is to formulate an expression for the net apparent brightness temperature emitted at the skin surface $T_{B.AP}$, as a function of T_{Bt}, the emissions from the intervening layers. $T_{AP.B}$ takes into account the net brightness contributions from all stratum (T_B (33)), as well as the down-welling ambient temperature T_{DN}. As described in [18], T_{DN} is attenuated by multiple reflections and losses in the tissue layers. By assuming, thermal equilibrium i.e. $T_{sk} = T_{ml} = T_{DN}$, T_{DN} can be equated to T_B, to resolve a second coefficient of multiple reflections denoted by CMR2 (34), yielding (35). Thus the final expression for $T_{B.AP}$ is presented in (36).

$$CMR2 = \frac{\left(1 - 2\Gamma_a\right)\left(\frac{\Gamma_{ml}}{L_{sk}L_{ml}} + \Gamma_a\right)}{1 - \frac{\Gamma_{ml}\Gamma_a}{\left(L_{ml}L_{sk}\right)^2}} \quad (34)$$

$$T_{DN} = T_{dn}CMR2 \quad (35)$$

$$T_{B.AP} = T_B + T_{DN} \quad (36)$$

6.3 Applying the TPM

By employing the formulas derived in section 6.2, the process of applying the TPM to the HCM is straightforward. $T_{B.AP}$ is a function of the reflections (Γ_t), electrical properties (α_t, L_t) and physical characteristics (δ_t, T_t) of the strata, where α_t is the attenuation constant, L_t is the loss, and δ_t the thickness of layer t. The calculated values for α_t, δ_t, Γ_t and L_t are provided in Table 9.

Illustrated in Figure 50 are the results from the comparison of the emitted brightness temperature calculated from $T_{B.AP}$ of the TPM in (36) to T'_{SKN}, the brightness temperature detected by the radiometer. The coherent based Wilheit model is also used in the comparison to show that coherent propagation effects can indeed be ignored [37]. This assumption is proved via the small percent between the TPM and Wilheit model (Figure 51). The similarities in the curves demonstrate that the radiometric measurement T'_{SKN} is analogous to that of the TPM ($T_{B.AP}$) and Wilheit models with percent error values on the order of 1% – 2.5%. Error values of this degree are quite impressive considering that the measurement is quite sensitive to many factors, as demonstrated in the analysis in section 5.2.1. For instance a 1 degree inaccuracy in the atmospheric temperature could yield error values on the order of 10% – 15%, as illustrated in Figure 44 of section 5.2.2.

Table 9. Calculated values of α_t, Z_t, Γ_t and L_t.

LAYER	Z (mm)	Γ (unitless)	α (m^{-1})	L (unitless)
BLOOD	40	0	34.66	19.45
MUSCLE	8	0.01	41.62	1.946
SKN	2	0.561	37.1	1.181

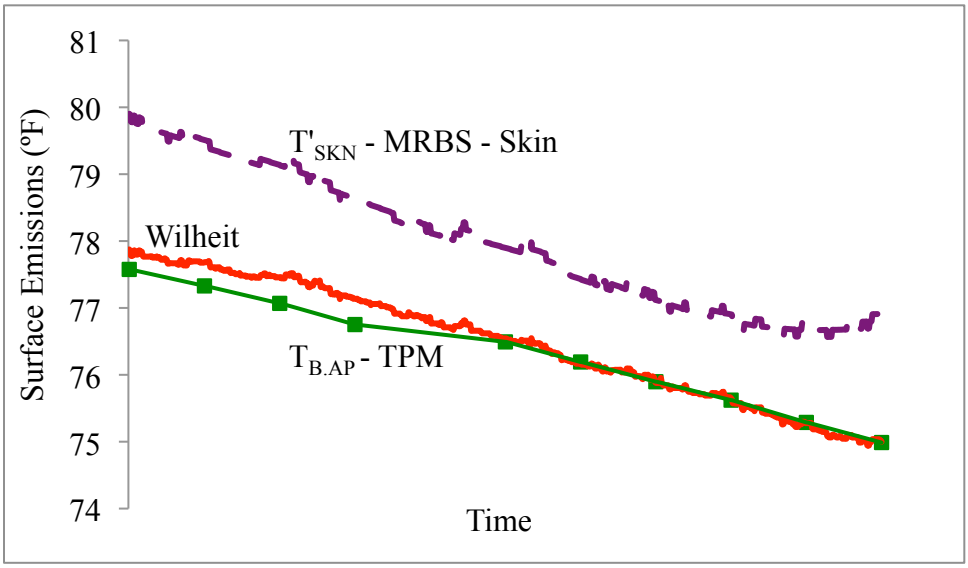

Figure 50. Emitted brightness temperature at the surface (Skin) of the HCP measured by the MRBS and compared to the TPM and Wilheit model.

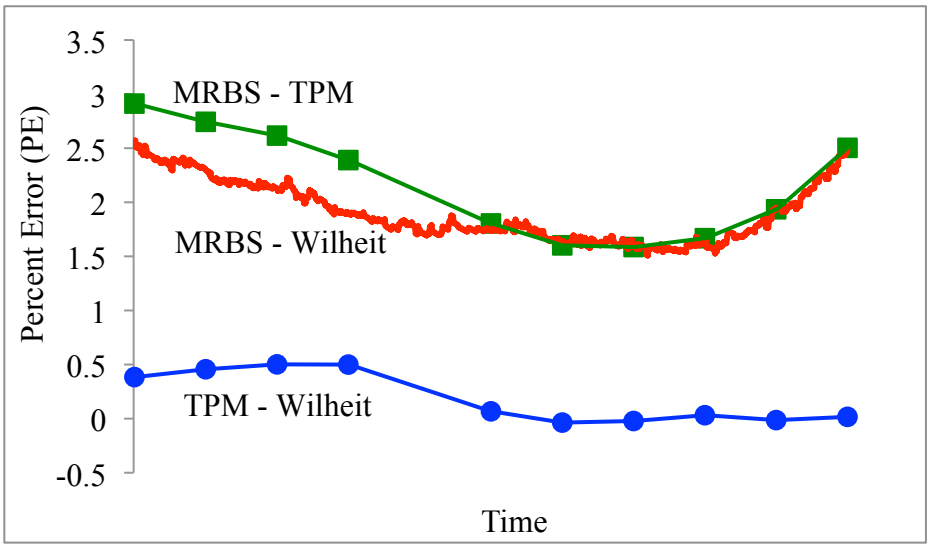

Figure 51. Percent error plots: MRBS – TPM, MRBS – Wilheit, Model and Wilheit – TPM.

6.4 Core Body Temperature Extraction

Ultimately, core temperature extraction is plausible by solving for T_{bl} in the $T_{B.AP}$ expression (37). α_t, δ_t, Γ_t and L_t are calculated from (21) – (22) as a function of the

layer thicknesses δ_t, which in practice can be estimated, based on the body fat percentage, weight, and height of the individual. The remaining unknowns are T_{sk} and T_{ml}, the physical temperatures of the skin, and muscle respectively. T_{sk} is typically a measurable quantity, monitored by an infrared thermometer. T_{ml} is resolved by applying heat transfer theory to the tissue layers and deriving a differential equation to express the heat transfer profile of T_{ml} as a function of T_{sk} and T_{bl}. Finally, T'_{SKN} can be substituted for the remaining unknown $T_{B.AP}$, since the two are analogous. With all of the remaining unknowns resolved, core body temperature is extracted by solving simply for T_{bl} in (37).

$$T_{bl} = \left(\frac{L_{ml}L_{sk}}{1-\Gamma_{ml}}\right)\left(\frac{T_{B.AP} - T_{B.sk} - T_{B.ml} - T_{DN}}{CMR}\right) \qquad (37)$$

6.5 Conclusion

This chapter presents a derivation of the TPM which is the final component for core body temperature extraction using microwave radiometry. The four level derivation is based on a similar procedure employed in [36] for net apparent brightness temperature of stratified dielectric media. The TPM is applied to the HCP and the results were compared to that of the radiometric measurement taken by the MRBS. The results were promising, yielding only marginal error, on the order of 1.5% - 2.5%. Such promising results infer that the extraction of core temperature can be achieved with high accuracy by implementing mathematical models to supplement the radiometric measurement, however certain parameters must be monitored to a high degree of accuracy.

CHAPTER 7

SUMMARY AND RECOMMENDATIONS FOR FUTURE WORKS

7.1 Summary

Presented is a microwave radiometer and associated design methods for non-invasive monitoring of core body temperature. The long term goal is to develop a multifunctional radiometric health monitoring system, deployable inside the uniforms of astronauts, with optimal functionality 2 cm – 4 cm from the body. Based on a review of the literature, we have identified certain drawbacks of the on-body approach which may be intolerable for the current application, therefore a non-contact modality is being investigated. This work demonstrates certain design considerations for the close proximity approach however, the most significant contributions lie within the areas of antennas and propagation.

We begin with a preliminary study, in which certain occurrences which obstruct the close proximity measurement have been identified. The antenna requirements for biomedical radiometric sensing were also presented. Based on these requirements, a half wavelength printed dipole (PD1) was selected for 1st generation sensor because it is a widely studied, compact, broadband aperture with a relatively simple design. However, when brought in close proximity to the body, the antenna characteristics are distorted in the form of resonance shifts, impedance mismatch and bandwidth degradation. These phenomena induce considerable degradation in the end to end system performance.

These obstructive artifacts are demonstrated empirically by characterizing the antenna in the near-field of RF tissue phantoms, which have been developed as the experimental test bed for measurement and testing purposes. Compared to traditional saline phantoms, the test bed in this study is comprised of tissue phantoms with electrical properties closer to that of human tissue, enabling more precise characterization of the antenna-body effects as related to sensor performance. Solutions in the area of antenna design are provided by implementing an absorbing cavity to suppress unwanted radiation opposite the specimen. However the antenna characteristics change when inside the cavity; therefore the antenna is reconfigured for cavity operation using common design techniques (impedance matching, frequency tuning). We have also discovered receiver instability issues which are represented by the variations in the slope of the calibration curves/equations, which is likely due to thermal drifts in the RF components.

Based on findings from the preliminary study, a 2nd generation design was developed which incorporates continuous calibration for receiver instabilities, an enhanced antenna design, and associated non-contact propagation model to correct for errors which arise due to the non-contacting nature of the sensor. The 2^{nd} generation sensor is 33% smaller than the 1^{st} generation design, which in turn improves the stability and resolution of the system. The 2^{nd} generation antenna is a cavity backed slot antenna (CBSA) designed for non-contact biomedical radiometric sending. Compared to the 1^{st} generation printed dipole antenna (PD1), the CBSA is more efficient and provides a considerable improvement in bandwidth ($B \geq +150$) MHz. The gain and directivity were also enhanced by at least 1.5 dB. By optimizing the antenna design parameters, the CBSA has been configured to meet the requirements for biomedical applications and

account for near field antenna – body effects. The antenna is broadband ($\geq$ 400 MHz) and very efficient (88%), enabling high sensor resolution. It is also a directional radiator, designed at 1.4 GHz for targeted detection of core body temperature emissions from depths of $\leq$ 27 mm. The internal feed enables tunability of 50 MHz/mm of the feed length and adds novelty to the design in biomedical applications by reducing the intensity of antenna feed currents which may interact with the body. Measurements and simulations of the antenna S11 in close proximity to the phantom are comparable, as well as the radiation patterns. From these results, it was concluded that the CBSA is a good candidate for biomedical sensing applications and best suited for the current application, relative to the PD1.

Although the CBSA enhances end-to-end performance of the system, a perfect antenna is not realizable, therefore a mathematical representation in the form of a non-contact model (NCM) was implemented to mitigate certain artifacts not accounted for in the antenna design. The model is presented in three phases for extraction of the measurement, corrections at the antenna interface, and a final correction at the critical air – tissue boundary.

Close proximity measurements were performed on the enhanced measurement test bed using the 2nd generation sensor and the results were processed at each stage of the NCM. The 2nd generation sensor is a microwave radiometer designed for biomedical sensing applications (MRBS). The enhanced test bed is a three layer human core model (HCM) which mimics the dielectric properties of a human stomach volume; skin, muscle, and blood-fatty tissue. As the blood temperature was varied within the range of normal body temperature and conditions of heat related disorders, the MRBS monitored the

brightness temperature of the HCM, while the physical temperatures were tracked using thermal probes positioned throughout the HCM. The measurement data was processed through the NCM and a sensitivity analysis was performed to determine which model parameters the measurement is most sensitive to. The results demonstrate that the measurement is most sensitive to atmospheric contributions and antenna impedance match, the latter being influenced by the presence of biological media. The close proximity measurement is less sensitive to the physical temperature of the antenna, which has been known to distort on-body measurements. Furthermore, minimal sensitivity to the antenna efficiency and main probing hemisphere enables antenna design flexibility. The measurement is least sensitive to the emissivity of the specimen, which implies that the MRBS performance will have negligible variation from person to person. It is important to note that proper shielding of the antenna and sensor from ambient noise is critical for achieving a highly accurate measurement. Ultimately, the correlation between the core temperature of the HCM and the extracted subsurface temperature was within 8% difference after applying the NCM.

With the goal of achieving a percent error of $\leq$ 3%, the accuracy of the measurement is further enhanced by developing a tissue propagation model (TPM) to account for losses and multiple reflections throughout the stratified tissue. The TPM is based on Ulaby's derivation of an expression for the net emissions from a multilayer medium with a non-uniform dielectric profile. Incoherency is assumed since propagation will be solely based on the power density of the propagating emissions, whereby phase effects are negligible. This assumption is mainly attributed to the fact that scattering will be minimal, due to the size of skin cells, as compared to the sensing wavelength. In

addition, the sensor is expected to remain relatively parallel with the tissue, which further negates phase and or angular dependence.

The TPM derivation is presented in four levels, beginning with a definition of the fundamental model components and complexity is added at each level, towards the complete derivation. First the emissions from the individual strata ($T_{s.t}$) are defined at level 1, with t representing the tissue layer; sk = skin, ml = muscle and bl = blood – fatty tissue. Next, the derivation of the up and down-welling emissions per layer, $T_{t.U}$ and $T_{t.D}$, are presented in level 2 which are combined at level 3, to make up the net apparent emissions from all strata (T_B). The atmospheric contributions (T_{DN}) are introduced at level 4 to complete the full derivation of the apparent brightness emission $T_{AP.B}$ radiated at the skin surface. Justification for the incoherent approach is demonstrated by comparing the TPM to the coherent Wilheit model, yielding percent error (PE) results of $\leq$ .5%. Thereafter the TPM response is correlated to the brightness temperature measurement of the HCM from the MRBS. The percent error between the two measurements was $\leq$ 3%. As a result, the MRBS measurement can be substituted for the output of the TPM, which provides an expression for the brightness temperature emissions measured at the skin surface, as a function of the subsurface tissue. Ultimately, this expression is used to extract core body temperature by solving for the remaining unknowns: 1) The loss (L_t), reflections (Γ_t), and attenuation (α_t) per layer (t) and are calculated based on the material properties; 2) the physical temperature of the skin (T_{sk}) is a measurable quantity which is typically monitored using an infrared thermometer; 3) the physical temperature of the muscle layer (T_{ml}) can be resolved using heat transfer theory by applying a system of differential equations at the tissue

boundaries; 4) at this point the remaining unknowns have been resolved and the inner core temperature T_{bl} can be extracted via first order linear equation.

7.2 Recommendations for Future Works

To achieve the long term goal of developing a real time, field deployable radiometric health monitoring system, we plan to continue this research with strong emphasis on optimizing the performance of the sensor, characterization of the antenna – body near field, and refining of the current tissue propagation model. The technical objectives are to: I) design a 3rd generation sensor with enhanced gain control, data processing techniques, and the capability of measuring changes in the emissivity of the specimen as well as temperature; II) perform an experimental study on the antenna – body effects using various near-field antennas to derive a model which characterizes the close-proximity electromagnetic effects, as a function of antenna offset distance; and III) refine the previously developed tissue propagation model to account for an additional tissue layer and perform a sensitivity analysis of the model parameters to determine the sensitivity of the measurement to different body types.

The rationale for the enhancements to the 3rd generation sensor are to measure the emissivity of the tissue, which changes as a function of temperature, and implement advanced design enhancements and averaging schemes. Correcting for emissivity error which results from temperature changes in the stratified tissue, is critical for optimal accuracy in non-contact as well as on-body radiometric sensor technologies [38]. This correction is trivial at the skin surface, however the level of difficulty is heightened as a function of the tissue depth. Therefore an additional Dicke "emissivity" standard will be

added to the third generation design. The concept is to monitor variations in the emissivity of the standard by changing its input mach until the radiometer is balanced, i.e. output = 0. This provides the emissivity profile of the tissue across the sensing depth. By adding the additional standard, there exists some degradation in resolution [39]. To offset this loss in performance, an additional automatic gain control stage will be implemented, which is expected to improve the accuracy of the sensor beyond our current percent error value of $\leq 3\%$ (see section 6.3). Additional data processing techniques will also be implemented since the calibration cycle of the current 2^{nd} generation design is approximately 1.4 s per measurement, whereas the system is capable of thousands of calibration cycles per second. Improving the frequency of calibration provides more measurement (data) samples, which can be averaged using advanced algorithms to improve the resolution of the sensor.

In an effort to better understand the antenna performance, as a function of the distance from the body, we plan to characterize the antenna-body near field, by resolving constants to fit a near-field propagation model. The design and development of directional antennas with optimal performance ($S11 \leq -20dB$, efficiency $\geq .85$) at short distances from the body is vital for the success of this project. In general, the characteristics of various near field antennas will be measured at various distances from the human core tissue phantom model to complete stage 3 of a two port network, whereas stage 1 is the electrical characteristics of the phantom model presented in section 3.5, and stage 2 is the antenna-body near field which is considered as the device under test (DUT). Genetic algorithms will be used to match the DUT to the electrical response of stage 3. Repeatability across the various antenna types will enable the extraction of the electrical

constants to derive the near field propagation model. This model will be used to design candidate antennas with characteristics that fit the model. The near-field model will also enable the design of feedback networks with automatic impedance matching integrated onto the candidate antennas. Proposed are conformal geometries such as fabric antennas that can be easily integrated into uniforms or miniaturized cavity antennas in which the sensor can be fully integrated as a hand held device.

To further improve the accuracy of the current TPM, we plan to add an additional layer which can be used to model, fatty and connective tissue such as cartilage. The derivation will follow a similar procedure to that of section 6.2. Thereafter a sensitivity analysis will be performed to determine the sensitivity of the measurement to different body types by changing the thickness and dielectric properties of the tissue within reasonable ranges for the human body. The exact values will be determined from a statistical analysis of data aggregated from an additional study which will be conducted to determine the thickness of the tissue layers of an abdominal cavity based on the height, weight, and age of the individual. The objective is to use the TPM to derive body standards for the sensor which can be generated by inputting the height, weight, and age of each user. In essence, this body type calibration customizes the sensor's measurement extraction algorithms for each individual user.

LIST OF REFERENCES

[1] W.J. Yang, S. Mochizuki, and P.T. Yang, "Applications of Microwave Radiation in Medicine," *Journal of Mechanics in Medicine and Biology*, vol. 2, pp. 53-63, October 2002

[2] F. Sterzer, "Microwave medical devices," *IEEE Microwave Magazine* vol. 3, pp. 65-70, March 2002

[3] A. Rosen, M.A. Stuchly, and A. Vander Vorst, "Applications of RF/microwaves in medicine," *IEEE Transactions on Microwave Theory and Techniques*, vol. 50, pp. 963-974, March 2002

[4] E. C. Fear, S. C. Hagness, P. M. Meaney, M. Okoniewski, and M. A. Stuchly, "Enhancing breast tumor detection with near-field imaging," *IEEE Microwave Magazine*, vol. 3, pp. 48-56, January 2002

[5] L.M. Burdina, I.G. Pinkhosevich, V.A. Khailenko, S.G. Vesnin, and N.N. Tikhomirova, "X-Ray Diagnostics and X-Ray Therapy in Clinic of XXI," *III Russian Scientific Forum,* pp. 49-50, 2002

[6] F, Bardati, and S. Iudicello, "Modeling the Visibility of Breast Malignancy by a Microwave Radiometer," *IEEE Transactions on Biomedical Engineering*, vol. 55, pp. 214-221, January 2008.

[7] L.R. Ballew, "A Microwave Radiometer for use in Biomedical Sensing Applications," Master's Thesis, Baylor University, 2006

[8] O. Jay, F.D. Reardon, P. Webb, M.B. Ducharme, T. Ramsa, L. Nettlefold, and G.P. Kenny, "Estimating changes in mean body temperature for humans during exercise using core and skin temperatures is inaccurate even with a correction factor," *Journal of Applied Physics*, vol., pp. 443–451, 2007

[9] E. C. Green, "Design of a microwave sensor for non-invasive determination of blood-glucose concentration," Master's Thesis, Baylor University 2005.

[10] A.T. Oikonomou, I.S. Karansiou, and N.K. Uzunogu, "Conformal Patch antenna for human brain imaging using near field radiometry," *5th European Symposium on Biomedical Engineering,* 2006

[11] S. Jacobsen, and P. Stauffer, "Performance Evaluation of Various Antenna Configurations for Microwave Thermography During Superficial Hyperthermia," *Journal of Electromagnetism Waves and Applications,* vol. 15, no. 1, pp. 111-134, 2001

[12] I.S. Karanasiou, A.T. Oikonomou and N.K.Uzunoglu "Potential brain imaging using near field radiometry," *4th International Conference on Imaging Technologies in Biomedical Sciences*, September 2007

[13] I.S. Karanasiou, K.T. Karathanasis, A. Garetsos A and N.K. Uzunoglu "Development and laboratory testing of a noninvasive intracranial focused hyperthermia system," *IEEE Transactions on Microwave Theory and Techniques*, vol. 56, pp. 2160–2171, September 2008

[14] K.L. Carr, "Antenna: the critical element is successful medical technology," *IEEE MTT-S International Microwave Symposium Digest*, vol. 1, pp. 525-527, May 1990

[15] P. Racette, and R. H. Lang, "Radiometer design analysis based upon measurement uncertainty," *Radio Science*, vol. 40, 2005 RS5004, doi:10.1029/2004RS003132

[16] K.-J.C. Tien, J. Judge, and R.D. de Roo, "Comparsion of different microwave radiometric calibration techniques," *IEEE IGARSS*, vol. 6, pp 3748-3751, 2004

[17] K.D. Stephan, and J.A. Pearce, "Antennas and reflectors for near-field radiometric remote sensing of temperature in industrial applications," *IEEE Antennas and Propagation Society International Symposium*, vol. 4, pp. 302 – 305, August 2002

[18] F.L. Ulaby, R.K. Moore, and A.K. Fung, Microwave Remote Sensing, Active and Passive, vol. 1, pp. 354-356, Artech House Inc, 1981

[19] S. Jacobsen, and P. Stauffer, "Performance Evaluation of Various Antenna Configurations for Microwave Thermography During Superficial Hyperthermia," *Journal of Electromagnetism Waves and Applications*, vol. 15, no. 1, pp. 111-134, 2001

[20] W.J. Yang, S. Mochizuki and P.T. Yang "Applications of Microwave Radiation in Medicine," *Journal of Mechanics in Medicine and Biology*, vol. 2, pp 53-63, October 2002

[21] T.L. Chen, "Printed Circuit Board Dipole Antennas and Dipole Antenna Array Operating at 1.8GHz," B.S. Thesis, University of Cape Town, 2003

[22] Q. Bonds, T. Weller, B. Roeder and P. Herzig, "A tunable Cavity Backed Slot Antenna (CBSA) for close proximity biomedical sensing applications," *IEEE Microwaves, Communications, Antennas and Electronics Systems*, 2009

[23] C. Gabriel, and S. Gabriel, "Compilation of the Dielectric Properties of Body Tissues at RF and Microwave Frequencies," Brooks AFB report number AL/OE-TR-1996-0037, 1996

[24] Australian Communication Authority, "Radiocommunications (Electromagnetic Radiation Human Exposure) Standard 2003," Radio Communications Act, 1992 Section 162, June 2003

[25] American Sports Education Program (ASEP) "Heat Related Disorders," 2001 http://www.khsaa.org/sportsmedicine/heat/hkheatrelateddisorders.pdf

[26] G. Breed, "Design Issues for Direct-Conversion Wireless Radios," *High Frequency Electronics,* vol. 2, no. 6, pp. 48 – 51, June 2004

[27] N. V. Larsen, and O. Breinbjerg, " An L-Band, Circularly Polarized Dual-Feed, Cavity-Backed Annular Slot Antenna for Phased-Array Applications," *Microwave and Technology Letters*, vol. 48, pp. 873-878, May 2006

[28] T. Yilmaz, T. Karacolak, and E. Topsakal, "Characterization of Skin Mimicking Gels for Implantable Antennas Operating at ISM Band (2.4 GHz - 2.48 GHz)," *National Radio Science Meeting URSI*, 2008

[29] K. Ito, "Numerical and Experimental Human Body Phantoms," *IEEE IET Seminar on Antennas and Propagation for Body-Centric Wireless Communications*, 2007

[30] M.S. Hawley, J. Conway, A.P. Anderson, and P.A. Cudd, "The influence of tissue layering on microwave thermographic measurements," *International Journal of Hyperthermia*, vol. 4, no. 4, pp. 427-435, July 1988

[31] C. L. Lim, C. Bryn, and J.K.W. Lee, "Human thermoregulation and measurement of body temperature in exercise and clinical settings," *Annals Academy of Medicine*, vol. 4, pp. 347-353, April 2008

[32] Q. Bonds, J. Gerig, T. Weller, and B. Roeder, "Towards Core Body Temperature Measurement via Close Proximity Radiometric Sensing," *IEEE Sensors Journal, Special Issue on Non-Invasive Physiological Monitoring,* submitted August 2010

[33] F.L. Ulaby, R.K. Moore, and A.K. Fung, Microwave Remote Sensing, Active and Passive, vol 1., pp. 204-210, Artech House Inc, 1981

[34] J.D. Jackson, "How the antenna launches its power into radiation: The pattern of the Poynting vector at and near the antenna," The American Journal of Physics, vol. 74, pp. 280-288, April 2006

[35] Q. Bonds, T. Weller, B. Roeder and P. Herzig, "A Total Power Radiometer (TPR) and Measurement Test Bed for Non Contact Biomedical Sensing Applications," *IEEE Wireless and Microwave Technology Conference,* 2009

[36] F.L. Ulaby, R.K. Moore, and A.K. Fung, Microwave Remote Sensing, Active and Passive, vol 1., pp. 236-244, Artech House, 1981

[37] T. T. Wilheit, "Radiative transfer in a plane stratified dielectric," *IEEE Transactions on Geoscience and Remote Sensing*, vol. 16, pp. 138-143, 1978

[38] F. Sterzer, "Temperature-measuring microwave radiometer apparatus," U.S. Patent 5949845, September 1999

[39] N. Skou and D. L. Vine, *Microwave Radiometer Systems Design and Analysis* second edition, Artech House Inc, 2006.